NKG7 Is a T-cell–Intrinsic Therapeutic Target for Improving Antitumor Cytotoxicity and Cancer Immunotherapy

Ti Wen[1], Whitney Barham[2], Ying Li[3], Henan Zhang[1], Joanina K. Gicobi[2], Jacob B. Hirdler[1], Xin Liu[1], Hyoungjun Ham[2], Kodi E. Peterson Martinez[2], Fabrice Lucien[1], Roxane R. Lavoie[1], Hu Li[4], Cristina Correia[4], Dileep D. Monie[2], Zesheng An[1], Susan M. Harrington[1], Xiaosheng Wu[5], Ruifeng Guo[6], Roxana S. Dronca[7], Aaron S. Mansfield[8], Yiyi Yan[8], Svetomir N. Markovic[8], Sean S. Park[9], Jie Sun[2,10], Hong Qin[11], Minetta C. Liu[8], George Vasmatzis[12], Daniel D. Billadeau[2], and Haidong Dong[1,2]

ABSTRACT

Cytotoxic CD8$^+$ T cells (CTL) are a crucial component of the immune system notable for their ability to eliminate rapidly proliferating malignant cells. However, the T-cell intrinsic factors required for human CTLs to accomplish highly efficient antitumor cytotoxicity are not well defined. By evaluating human CD8$^+$ T cells from responders versus nonresponders to treatment with immune checkpoint inhibitors, we sought to identify key factors associated with effective CTL function. Single-cell RNA-sequencing analysis of peripheral CD8$^+$ T cells from patients treated with anti–PD-1 therapy showed that cells from nonresponders exhibited decreased expression of the cytolytic granule-associated molecule natural killer cell granule protein-7 (*NKG7*). Functional assays revealed that reduced NKG7 expression altered cytolytic granule number, trafficking, and calcium release, resulting in decreased CD8$^+$ T-cell–mediated killing of tumor cells. Transfection of T cells with *NKG7* mRNA was sufficient to improve the tumor-cell killing ability of human T cells isolated from nonresponders and increase their response to anti–PD-1 or anti–PD-L1 therapy *in vitro*. *NKG7* mRNA therapy also improved the antitumor activity of murine tumor antigen–specific CD8$^+$ T cells in an *in vivo* model of adoptive cell therapy. Finally, we showed that the transcription factor ETS1 played a role in regulating NKG7 expression. Together, our results identify NKG7 as a necessary component for the cytotoxic function of CD8$^+$ T cells and establish NKG7 as a T-cell–intrinsic therapeutic target for enhancing cancer immunotherapy.

See related article by Li et al., p. 154.

Introduction

Cytotoxic CD8$^+$ T cells (CTL) are a crucial component of the immune system. They are capable of specifically targeting and eliminating malignant tumor cells throughout the body (1). To accomplish this, CTLs are first primed by antigen-presenting cells in secondary lymphoid organs and then traffic to the tumor site where they encounter their cognate antigen on the tumor cell itself. This triggers the initiation of an immune synapse followed by exocytosis of cytolytic granules containing perforin and granzymes, which results in tumor-cell destruction. The coordination of the cytolytic killing machinery within CD8$^+$ T cells is multi-faceted and complex, involving numerous proteins as well as the filamentous actin (F-actin) and microtubule cytoskeletons to ensure directed delivery of lytic granules to the contact site formed between the CD8$^+$ T cell and the tumor target (2, 3). Although extrinsic factors within the tumor microenvironment that affect T-cell killing have been well studied in the context of immune checkpoints or regulatory cells (4, 5), the T-cell intrinsic factors that are required for human CTLs to achieve and maintain highly efficient antitumor cytotoxicity are still not well defined.

This gap in knowledge has become particularly apparent now that there are a variety of immune-modulating agents used therapeutically, all of which are designed to enhance CTL responses against tumors. The ultimate goal of tumor vaccines, chimeric antigen receptor (CAR) T-cell methodologies, and immune checkpoint inhibitors is to produce CTLs that can efficiently eliminate tumor cells. However, no consensus exists as to what defines the specific subset of effector CD8$^+$ T cells responsible for the "best" tumor-cell killing or what components need to be present within CTLs to get the most robust antitumor response.

PD-1/PD-L1–binding mAbs are among the most widely used of these cancer immunotherapies and treatment with these agents can lead to complete remission in a small proportion of patients. Unfortunately, the majority of patients treated experience no detectable

[1]Department of Urology, Mayo Clinic, Rochester, Minnesota. [2]Department of Immunology, Mayo Clinic College of Medicine and Science, Rochester, Minnesota. [3]Division of Computational Biology, Mayo Clinic, Rochester, Minnesota. [4]Center for Individualized Medicine, Department of Molecular Pharmacology and Experimental Therapeutics, Mayo Clinic College of Medicine and Science, Rochester, Minnesota. [5]Division of Hematology, Mayo Clinic College of Medicine and Science, Rochester, Minnesota. [6]Department of Laboratory Medicine and Pathology, Division of Anatomic Pathology, Mayo Clinic, Rochester, Minnesota. [7]Division of Medical Oncology, Mayo Clinic, Jacksonville, Florida. [8]Division of Medical Oncology, Mayo Clinic, Rochester, Minnesota. [9]Department of Radiation Oncology, Mayo Clinic, Rochester, Minnesota. [10]Division of Pulmonary and Critical Care Medicine, Mayo Clinic, Rochester, Minnesota. [11]Division of Hematology and Oncology, Mayo Clinic, Jacksonville, Florida. [12]Department of Molecular Medicine, Mayo Clinic, Rochester, Minnesota.

T. Wen, W. Barham, and Y. Li contributed equally to this article.

Corresponding Author: Haidong Dong, 200 1st Street SW, Rochester, MN 55905. Phone: 507-284-5482; E-mail: dong.haidong@mayo.edu

Cancer Immunol Res 2022;10:162–81

doi: 10.1158/2326-6066.CIR-21-0539

This open access article is distributed under the Creative Commons Attribution-NonCommercial-NoDerivatives 4.0 International (CC BY-NC-ND 4.0) license.

©2021 The Authors; Published by the American Association for Cancer Research

clinical response (6, 7). Although the initial mechanism of action of PD-1/PD-L1 blockade was thought to be the rescue of exhausted T cells within the tumor microenvironment, more recent studies point to the importance of T-cell proliferation in the periphery after treatment (8–10). These peripheral T-cell clones then infiltrate the tumor and are likely responsible for tumor killing. It has been shown that in both responders and nonresponders, distinct modules of genes associated with therapy are induced within peripheral $CD8^+$ T cells, including those involved in cell division. Still, in nonresponders, this does not lead to a measurable decrease in tumor burden (11, 12). This cannot be fully explained by a failure of T cells to infiltrate tumors, as even some so called "hot" tumors with molecular signatures that belie significant T-cell infiltration do not respond to anti–PD-1 therapy (13, 14). Thus, we hypothesized that there are additional T-cell intrinsic factors necessary for effective tumor-cell killing that are deficient in the T cells of nonresponders. If these factors could be identified, they would not only offer insight into how to optimize CTL function for adoptive cellular therapy (ACT) but could also potentially be restored in $CD8^+$ T cells to overcome resistance to PD-1/PD-L1 checkpoint inhibition.

Herein, we employed single-cell RNA-sequencing (scRNA-seq) technology to analyze $CD8^+$ T cells from the peripheral blood of complete responders (no tumor measurable at the time of posttreatment sampling) and nonresponders to anti–PD-1 therapy, comparing differential gene expression across time [baseline (BL) vs. postinitiation of treatment (PT)] and, in a second analysis, gene expression within the largest and most expanded T-cell clones. This investigation highlighted that appropriate expression of a cytolytic granule associated molecule, natural killer cell granule protein-7 (NKG7), was a feature of the cytotoxic $CD8^+$ T cells within complete responders to anti–PD-1 therapy. We further characterized NKG7 within human primary $CD8^+$ T cells and uncovered its role in cytolytic granule trafficking and release. To begin translating this knowledge to a potential therapy, we used mRNA transfection to modulate *NKG7* expression within the $CD8^+$ T cells of nonresponders. This was sufficient to improve cytolytic T-cell killing of tumor cells *in vitro* and increase their response to PD-1/PD-L1 blockade. *NKG7* mRNA therapy also improved the antitumor activity of murine tumor antigen–specific $CD8^+$ T cells *in vivo* in a model of ACT. Finally, we considered how *NKG7* expression may be modulated at the transcription level. Together, our results have identified NKG7 as a necessary T-cell intrinsic factor for the cytotoxic function of $CD8^+$ T cells and established NKG7 as a new therapeutic target for cancer immunotherapy.

Materials and Methods

Study design

This study was performed to identify gene expression differences within the $CD8^+$ T cells of responders versus nonresponders to anti–PD-1 therapy with the goal of modulating the identified targets to improve response. This objective was addressed by (i) performing scRNA-seq analysis of 16 paired patient samples, taken from BL and posttreatment timepoints (before and after initiation of therapy), (ii) determining that reduced *NKG7* was a common feature among nonresponders and validating this finding in separate sets of patient data (protein-based and primary tumor-based studies), (iii) characterizing the function of NKG7 in human $CD8^+$ T cells by knockdown of *NKG7* in primary cells followed by cytotoxicity assays, time-lapse imaging studies, electron microscopy, and calcium-flux measurements, (iv) studying the effect of overexpression of NKG7 through transfection with *NKG7* mRNA on both human patient samples taken from nonresponding patients and on antigen-specific $CD8^+$ T cells from mice (*in vivo* modeling), and (v) screening for transcription factors that modulate *NKG7* gene expression through siRNA-mediated knockdown of transcription factors followed by chromatin immunoprecipitation qPCR (ChIP-qPCR), qRT-PCR, Western blot, and functional cytotoxicity assays. Sample size was determined by the investigators according to previous experimental experience. The exact *n* numbers used in each experiment are indicated in the respective figure legends. Samples were allocated randomly whenever possible. For mouse experiments, the mice were randomized at day 5 posttumor injection, upon first tumor measurement, such that all groups had similar averaged tumor sizes prior to treatment. Lab members performing caliper measurements of mouse tumors were blinded to treatment group. No data was excluded from the analysis. Outliers were included in statistical analyses and are represented in the graphs (all formatted as dot plots so that variations between individual patients, healthy donors, or mice can be clearly evaluated).

Human samples

All human participants provided signed informed written consent; the study was approved by the Mayo Clinic Rochester institutional review board (IRB) and was conducted according to Declaration of Helsinki principles. Peripheral blood and tumor tissue samples from patients were collected at either BL (prior to therapy) or PT after written consent was obtained from each participant (adults of both genders and all races). Clinical course, treatment information, and outcomes in patients treated with anti–PD-1/PD-L1 therapy at Mayo Clinic were retrospectively collected. Response to treatment was evaluated according to standard clinical practice guidelines using RECIST (15). An overview of the patient samples used in the study is provided in Supplementary Table S1 and details for the 8 patients whose samples were analyzed via scRNA-seq are available in Supplementary Table S2. The response listed [complete response (CR) vs. progressive disease (PD)] was apparent (using RECIST) at the 12-week PT timepoint for all patients, except for sample R-3, who was still categorized as PD at 12 weeks PT but had a CR overall (noted at 24 weeks PT). "Healthy Donor" human blood leukocytes were acquired from anonymous donors who had consented for blood donation at the Blood Transfusion Center at Mayo Clinic.

Processing of peripheral blood samples

Peripheral blood mononuclear cells (PBMC) were isolated from patient blood samples via centrifugation with lymphoprep (catalog no. 07851, StemCell Technologies) and SepMate conical tubes (catalog no. 85450, StemCell Technologies). Samples were then stored in liquid nitrogen for later use and thawed on the day of the experiments. PBMCs were isolated from healthy donors using the same protocol as above but from buffy coat blood. Once PBMCs were obtained from healthy donor blood, $CD8^+$ T cells were isolated using a magnet-based $CD8^+$ T-cell isolation kit according to the manufacturer's protocol (catalog no. 19053, StemCell Technologies), and the cells were used immediately for experiments.

scRNA-seq data collection

Sample preparation

PBMCs from patient blood were thawed and stained with anti-CD45, anti-CD3, and anti-CD8 (antibody details are in Supplementary Table S3). $CD45^+CD3^+CD8^+$ cells were then sorted using a FACSAria II sorter (BD Biosciences) running FACSDiva v8.0.1 software. After sorting, cells were washed twice in 1 × PBS + 0.05% BSA

and immediately submitted to the Medical Genome Facility Genome Analysis Core for further processing.

3′ sequencing methods (samples NR-1, NR-2, R-1, R-2)

The cells were first counted and measured for viability using the Vi-Cell XR Cell Viability Analyzer (Beckman-Coulter) and a basic hemocytometer and light microscope. Barcoded Gel Beads were thawed from −80°C to room temperature and the cDNA master mix was prepared according to the manufacturer's instructions for Chromium Single Cell 3′ v2 library & Gel bead kit or A-Chip kit (catalog no. PN-120237 or PN-120236, 10x Genomics). The target capture number of cells was 2,000 to 3,000, so a volume containing more than 5,000 live cells was combined with cDNA master mix. The cell suspension and master mix, thawed Gel Beads and partitioning oil were added to a Chromium Single Cell A chip. The filled chip was loaded into the Chromium Controller, where each sample was processed and the individual cells within the sample were captured into uniquely labeled Gel Beads-In-Emulsion (GEM). The GEMs were collected from the chip and taken to the bench for reverse transcription, GEM dissolution, and cDNA clean-up. The resulting cDNA was a pool of uniquely barcoded molecules. Cleaned and measured pooled cDNA continued on to library construction, where standard Illumina sequencing primers and a unique i7 Sample index were added to each cDNA pool.

All cDNA pools and resulting libraries were measured using Qubit High Sensitivity assays (Thermo Fisher Scientific, catalog no. Q32851), Agilent Bioanalyzer High Sensitivity chips (Agilent, catalog no. 5067–4626), and Kapa DNA Quantification reagents (Kapa Biosystems, catalog no. 07960298001). Libraries were sequenced at 60,000 fragment reads per cell following Illumina's standard protocol using the Illumina cBot and HiSeq 3000/4000 PE Cluster Kit (Illumina, catalog no. PE-410–1001). The flow cells were sequenced as 100 × 2 paired-end reads on an Illumina HiSeq 4000 using HiSeq 3000/4000 sequencing kit (Illumina, catalog no. FC-410–1002 and FC-410–1001) and HCS v3.3.52 collection software. Base-calling was performed using Illumina's RTA version 2.7.3.

5′ and single-cell V(D)J sequencing methods (samples NR-3, NR-4, R-3, R-4)

Initial processing was as described in 3′ sequencing methods. The resulting cDNA created a pool of uniquely barcoded molecules that were used to generate 5′ gene expression libraries and enriched T-cell receptor (TCR) libraries. Not more than 50 ng mass of cDNA sample was used to create a gene expression library. A much lower amount of cDNA was required to build a TCR enriched library. During library construction, standard Illumina sequencing primers and a unique i7 Sample index (10× Genomics, catalog no. PN-120262) were added to each cDNA pool (gene expression and TCR). As above, all cDNA pools and resulting libraries were measured using Qubit High Sensitivity assays (Thermo Fisher Scientific, catalog no. Q32851), Agilent Bioanalyzer High Sensitivity chips (Agilent, catalog no. 5067–4626), and Kapa qPCR DNA Quantification reagents (Kapa Biosystems, catalog no. 07960298001). Gene expression libraries were sequenced at 50,000 fragment reads per cell and TCR libraries were sequenced at 5,000 fragment reads per cell. Sequencing steps followed Illumina's standard protocol using the Illumina cBot and HiSeq 3000/4000 PE Cluster Kit (Illumina, catalog no. PE-410–1001). The flow cells were sequenced as 100 × 2 paired end reads on an Illumina HiSeq 4000 using HiSeq 3000/4000 sequencing kit (Illumina, catalog no. FC-410–1002 and FC-410–1001) and HCS v3.3.52 collection software. Base-calling was performed using Illumina's RTA version 2.7.3.

scRNA-seq data analysis

Generation of scRNA-seq data matrix and TCR clonotypes

10X Genomics Cell Ranger Single Cell Software Suite (v3.1.0) was used to demultiplex raw base call (BCL) files generated from the sequencer into FASTQ files. Cell scRNA-seq data and TCR sequencing data were aligned and quantified using Ranger count and Cell Ranger vdj protocols, respectively, against their corresponding GRCh38 human reference genome downloaded from 10X Genomics website.

Further analysis

We used the Seurat package (v3.1; RRID:SCR_007322; refs. 16, 17) to perform integrated analyses of single cells. Genes expressed in less than 3 cells and cells that expressed less than 200 genes and more than 40% mitochondria genes were excluded for downstream analysis in each sample. For scRNA-seq analysis, we followed the Seurat SCTransform integration workflow and the comparative analysis workflow. Each dataset was SCTransform-normalized and the top 3,000 Highly Variable Genes (HVG) across cells were selected. The datasets were integrated based on "anchors" identified between datasets before principal component analysis (PCA) was performed to do linear dimensional reduction. Shared Nearest Neighbor (SNN) Graph was constructed to identify clusters on the low-dimensional space [top 30 statistically significant principal components (PC)]. Enriched marker genes in each cluster conserved across all samples were identified, and differentially expressed genes between two selected conditions were detected using the default Wilcoxon rank-sum test at cluster level or patient sample level. A resolution of 0.06 was selected for R-1, R-2, NR-1, and NR-2 datasets (8-sample integration). Paired integration analysis (PT vs. BL) was also performed individually for each patient sample (R-1, R-2, NR-1, and NR-2) with a common resolution of 0.1. A resolution of 0.08 was used for R-3, R-4, NR-3, and NR-4 datasets (8-sample integration analysis). Integration analyses of scRNA-seq data and single-cell TCR data were performed first based on cell barcodes from the top five clones (by clone size) mapped to those in gene expression data. A second analysis was completed to consider expanded clones. Clones were considered "expanded" if the clone was detected in more cells in the PT sample versus the BL sample for an individual patient. Cells with expanded clones (size ≥ 10 in PT samples) were selected for differential gene expression analysis (responders vs. nonresponders). Total number of expanded clones in each sample: NR-3 = 8; NR-4 = 21; R-3 = 18; R-4 = 3.

Velocity analysis of RNA expression

Velocyto.py (v0.17.16; ref. 18) was used to generate a loom file for each sample with expressed repetitive elements masked. RNA velocity analysis was performed using the scVelo package (v0.2.3; ref. 19) by the dynamic modeling approach, and the dynamic RNA velocities were projected onto the Seurat integrated Uniform Manifold Approximation and Projection (UMAP) embedding.

Tumor biopsy NKG7 expression analysis

Primary tumor biopsies ($N = 47$; $n = 25$ responders, $n = 22$ nonresponders) were collected prior to immunotherapy treatment as part of an ongoing biorepository effort at Mayo Clinic (IMPRESS). RNA-sequencing (RNA-seq) libraries for tumor biopsy samples [melanoma and non–small cell lung cancer (NSCLC)] were prepared by a third party (TEMPUS) according to their platform. The RNA-seq paired-end sequence data was then rerun using MAP-RSeq version 3.0.0 (20), an integrated RNA-seq bioinformatics pipeline developed at the Mayo Clinic for comprehensive

analysis of raw RNA-seq paired-end reads. Normalized gene expression was calculated as explained previously (21). The abundance of *NKG7* mRNA was extracted from the normalized RNA-seq data and then subjected to ROC analysis, which was performed using the R package "Epi" version 2.40.

Flow cytometry of patient samples

PBMCs from patient samples were thawed, washed in complete RPMI (catalog no. 11875093, Gibco), and then resuspended in FACS buffer (1X PBS, 2 mmol/L EDTA, and 3% FBS; catalog no. 10437028, Gibco) at a concentration of 1×10^6 cells/100 μL (see Supplementary Table S4 for reagent details). Cells were then stained with antibodies for surface molecules for 30 minutes at 4 °C. Antibodies used were specific for CD3, CD8, PD-1, and CX3CR1 (see Supplementary Table S3). Cells were then washed once in FACS buffer and resuspended in Fixation Buffer (catalog no. 420801, Biolegend) for 20 minutes at 4°C. After fixation, cells were washed once with ICS Perm Wash Buffer (catalog no. 421002, BioLegend), and then stained for the intracellular molecule NKG7 (catalog no. 30-69AA, Epigentek) for 1 hour at 4°C in 100 μL of ICS Perm Wash Buffer. Following intracellular staining, cells were washed once with ICS Perm Wash Buffer and then resuspended in FACS buffer for flow cytometry analysis, which was completed on a Cytoflex LX (Beckman Coulter; DAQ Version: V2.233, MCB Version: V3.01) running CytExpert software (RRID:SCR_017217).

Cell lines

MCF-7, A375, Hut78, P815, and EL-4 cell lines were purchased as validated cell lines from ATCC (from 2010 to 2020) and cultured in supplemented DMEM. Aliquots of each cell line were cultured a maximum 30 days after being thawed. They have not been reauthenticated in the past year. B16-OVA cells were a kind gift from Dr. Richard Vile, Mayo Clinic, and were cultured in complete RPMI under selection with G4-18 (0.8 mg/mL; Gibco, catalog no. 11811-031). Further details regarding cell culture reagents can be found in Supplementary Table S4. All cell lines were assessed for *Mycoplasma* contamination via PCR and were negative.

Anti-NKG7 generation/purification

The rabbit polyclonal antibody to NKG7 (UniProtKB – Q16617) was obtained by immunizing a rabbit with keyhole limpet hemocyanin-conjugated NKG7 peptide DFWFEAVGPTHSAHSGLWPTGHGDI (Cocalico Biologicals). The anti-NKG7 polyclonal rabbit serum was affinity purified using Sulfolink (catalog no. 44895, Pierce Chemical) as per manufacturer's instructions. Supplementary Figure S1 shows that the NKG7 polyclonal antibody detects a single band at 17 kDa in wild-type (WT) $CD8^+$ primary T cells but does not detect the same band in NKG7 knockout (KO) cells, validation of its specificity. The full membrane of this blot can be found in Data File S1.

High-resolution confocal microscopy

Expanded $CD8^+$ T cells were washed once in serum-free (SF) RPMI, resuspended with SF-RPMI at 1.5 million cells/mL, and rested in a cell culture incubator (37°C, 5% CO_2) for 10 minutes. 180,000 cells were plated directly on 18-mm round coverslips (catalog no. 1.5; Electron Microscopy Sciences) precoated with poly-L-lysine [0.1% in H_2O (w/v); MilliporeSigma, catalog no. P8920) and incubated in a cell culture incubator for 2 minutes. Cells on coverslip were then fixed with 4% paraformaldehyde (PFA) in PBS for 18 minutes and permeabilized with 0.15% Triton-X 100 in PBS for 4 minutes at room temperature. Coverslips were stained with antibodies specific for NKG7, LAMP1 (Santa Cruz; clone H4A3), or perforin (BD Biosciences; clone δG9) antibodies, followed by donkey anti-mouse IgG or donkey anti-rabbit IgG antibodies conjugated with Alexa Fluor-488 (Thermo Fisher, catalog no. A21202; A21206) or Alexa Fluor-568 (Thermo Fisher Scientific, catalog no. A10037; A10042). Polymerized F-actin was detected using Alexa Fluor-647–conjugated phalloidin (Thermo Fisher Scientific, catalog no. A22287). Coverslips were mounted on glass slides using Antifade mounting reagent (VectorLabs, catalog no. 1000-10). NKG7 colocalization with LAMP1 and perforin was examined using an Airyscan-equipped LSM800 confocal microscope with a 63X oil immersion objective of NA 1.4 (Zeiss). Z-stack images containing 6 to 10 single T cells were taken in each experiment, and experiments were independently repeated twice. Acquired raw images were processed with Airyscan on Zen Blue software (version 2.6; Zeiss) and exported to tiff format. Colocalization analysis among NKG7, LAMP1, and perforin in expanded $CD8^+$ T cells was performed and automated using a customized macro program within ImageJ (version 1.45s; NIH; RRID:SCR_003070). For each channel, maximum intensity projection images were generated from z-stack images. A whole cell region was then defined as the area enclosed by NKG7 fluorescence. Pearson correlation coefficient between two fluorescence channels within a cell was calculated using a Coloc2 plug-in within ImageJ with the Costes automatic threshold setting (22).

NKG7 siRNA transfection of human $CD8^+$ T cells

Human $CD8^+$ T cells were isolated from healthy donors (see "Processing of peripheral blood samples") and then centrifuged at $200 \times g$ for 10 minutes prior to nucleofection (4D nucleofector system, Lonza). 10 million cell aliquots were combined with 500 pmol/L siRNA (siControl or siNKG7) in 100 μL P3 Buffer (Lonza Kit, catalog no. V4XP-3024) per nucleocuvette. Program FI-115 was used. Following transfection, cells were transferred to RPMI media (no FBS, no cytokines) for recovery. After 4 hours, warmed media was added such that each well contained RPMI with 10% FBS, rhIL2: 10 U/mL, rhIL15: 10 ng/mL, and rhIL7: 10 ng/mL (reagent details in Supplementary Table S3). The next morning, cells were stimulated as indicated in each experiment.

Control siRNA: ON-TARGETplus Nontargeting pool (catalog no. D-001810-10-20, Dharmacon)

NKG7 siRNA: SMARTpool ON-TARGETplus (catalog no. L-016047-00-0020, Dharmacon)

To measure the efficiency of *NKG7* knockdown, cells were transfected as described above, activated with anti-CD3/anti-CD28 beads (catalog no. 11132D, Gibco), and collected at 48 hours postactivation in RLT buffer (Qiagen, catalog no. 79216). RNA was then isolated using Qiagen RNeasy Plus Mini Kit (catalog no. 74134). Reverse transcription-reaction was completed using SuperScript III Reverse Transcriptase (catalog no. 18080–400, Invitrogen) and 200 ng of RNA template per sample. qRT-PCR analysis was completed using a QuantStudio 3 Real-Time PCR System (Applied Biosystems) and TaqMan Fast Advanced Master Mix (catalog no. 444455, Applied Biosystems). Taqman assays included: *NKG7* (Hs01120688-gl) and *18S* as a control (Hs99999901-Sl), both from Applied Biosystems. All samples were run in triplicate. Relative expression was calculated using the $2^{-\Delta Ct}$ method.

Western blots

$CD8^+$ T cells from healthy donors were pelleted via centrifugation at 3,000 rpm for 15 minutes and then lysed in NP-40 buffer (20 mmol/L Tris-CL, pH 8.0, 137 mmol/L NaCl, 10% glycerol, 1% NP-40, 2 mmol/L

EDTA) and concentrations measured via protein assay using Bio-Rad reagent (catalog no. 500-0006). Once diluted to equal concentrations, samples were combined with Laemmli sample buffer (Bio-Rad, catalog no. 1610747) and run using a Mini-PROTEAN Electrophoresis and Transfer system (Bio-Rad, catalog no. 1658004). Membranes were incubated with primary antibody overnight at 4°C (antibodies used were specific for NKG7, β-actin, ETS-1, or GAPDH; details listed in Supplementary Table S3). Secondary antibodies were added the next morning for 1 hour [horseradish peroxidase (HRP)–conjugated anti-rabbit and anti-mouse; details in Supplementary Table S3]. Signal was visualized using SuperSignal West Pico PLUS Chemiluminescence Substrate Kit (catalog no. 34577, Thermo Fisher Scientific) on a Syngene G:Box Chemi XX6 system running GeneSys software (V1.6.1.0; RRID:SCR_015770). Images were formatted for figures using Microsoft PowerPoint (Microsoft Office 2016). Full images are included in the Supplementary Data File S1.

Calcein release cytotoxicity assay

Target tumor cells were labeled with Calcein-AM (5 μmol/L, catalog no. C1430, Invitrogen) for 30 minutes of incubation at 37°C in dark, shaking occasionally, washed with Hank's Balanced Salt Solution (HBSS) twice and resuspended at 1×10^5/mL in RPMI. Human PBMC or $CD8^+$ T cells and target cells were mixed together at indicated target to effector ratios in RPMI without FBS and seeded into wells of a 96-well U-bottom plate. Saponin (0.1%) or Triton X-100 (2%) were added to wells that contained only tumor cells to provide a value for "maximum calcein release." In addition, tumor cell–only wells with no treatment were included to measure spontaneous release of calcein and media-only wells to measure background. All experimental and control conditions were performed in triplicate wells. The plate was briefly centrifuged at 1,000 rpm for 30 seconds, then incubated at 37°C for 4 hours. After 4-hour incubation, the plate was centrifuged at 2,000 rpm for 5 minutes. Hundred microliters of the 200-μL supernatant was then removed from each well and added to a new, opaque (black) 96-well flat-bottom plate (catalog no. 237105, Thermo Fisher Scientific). Calcein fluorescence was read using an automated fluorescence measurement system (BioTeK Synergy HTX multi-mode reader) with an excitation of 485 × 20 and an emission filter of 530 × 25, scanning for 1 second per well. Read-outs were exported to Microsoft Excel files (RRID:SCR_016137; Microsoft Office 2016) and percent cytotoxicity was then calculated using the following formula:

(Value of media-only wells (background) was first subtracted from all wells)
% Cytotoxicity = 100 × [(Experimental well release-Spontaneous release well)/(Maximum release well-Spontaneous release well)].

Transmission electron microscopy

$CD8^+$ T cells isolated from healthy donors were activated with anti-CD3/CD28 beads (catalog no. 11132D, Gibco) for 48 hours. After 48 hours, beads were removed using a magnet. $CD8^+$ T cells were then combined with MCF7 tumor cells at a ratio of 1:5 (Target:T cell), spun at 20 × *g* for 1 minute and then cultured for 1 hour at 37°C. The cocultures were then gently spun at 20 × *g* for 1 minute at 4°C with no brake. The cells were fixed in 1% osmium tetroxide (catalog no. 251755, Millipore Sigma) for 1 hour or at 4°C overnight, then postfixed for 1 hour in 1% osmium tetroxide. For transmission electron microscopy (TEM), the samples were dehydrated, embedded in Spurrs resin (catalog no. 14300; Low Viscosity Embedding Kit, Electronic Microscopy Sciences), sectioned at 90 nm, and observed using a Joel 1400 electron microscope (Joel USA Inc.). For quantification, images of individual tumor cell:T-cell interactions were printed and the number of granule structures within the T cells along the tumor cell:T-cell interface were counted manually by two different readers.

IHC staining of paraffin-embedded tissue

Tissue samples from human tonsils, metastatic melanoma in the small bowel, and squamous cell carcinoma of the tongue were originally fixed with 10% formalin for 48 hours at room temperature followed with ethanol tissue dehydration and replacement with Xylene before embedding tissues into paraffin blocks. The paraffin tissue sections were cut at 5-μm and deparaffinized with xylene and rehydrated with a graded series of ethanol. Slides were rinsed in distilled water and placed in Diva Decloaker 10X (catalog no. DV2004LX, Biocare Medical) antigen retrieval solution diluted to 1X. Slides were placed in Biocare Medicals pressure cooking Decloaking Chamber and heated to 121°C for 30 seconds then heated at 90°C for 10 seconds. Slides were removed from the chamber rinsed with running distilled water and incubated for 5 minutes in Dako TBS wash buffer (catalog no. S3006). All of the following steps were conducted at room temperature. Tissue sections were incubated for 10 minutes in PeroxiAbolish (catalog no. PXA969L, Biocare Medical), washed 2 × 5 minutes in wash buffer, incubated for 10 minutes in Background Sniper (catalog no. BS966L, Biocare Medical), and then washed 2 × 5 minutes in wash buffer. Sections were incubated for 2 hours in anti-human NKG7 rabbit polyclonal antibody diluted 1:500 in Renaissance Background Reducing Antibody Diluent (catalog no. PD905L, Biocare Medical; final concentration 1.56 μg/mL) and washed 3 × 5 minutes in wash buffer. Subsequently, slides were incubated for 10 minutes in rabbit probe (catalog no. M3R513H, Biocare Medical), washed 2 × 5 minutes and incubated 10 minutes in rabbit HRP polymer (Mach 3 anti-rabbit HRP polymer kit; catalog no. M3R513H, Biocare Medical) and washed 2 × 5 minutes. Staining was visualized with DAB (catalog no. BDB2004L, Biocare Medical) for three minutes. Slides were counterstained with hematoxylin (catalog no. 7211, Richard Allen-Scientific). Sections were blued in running tap water and dehydrated in a graded series of ethanol and cleared in xylene. Coverslips were mounted with Permount (catalog no. SP15-100, Thermo Fisher Scientific). An EVOS imaging system (Invitrogen) was used to capture images of slides with representative NKG7 staining.

Conjugate and time-lapse microscopy

$CD8^+$ T cells from healthy donors were isolated and transfected with siRNA, as described above, then cultured with anti-CD3/anti-CD28 beads. After 48-hour stimulation, $CD8^+$ T cells were collected (beads removed) and labeled with lysotracker (Red 555, Invitrogen, catalog no. L7528) for 1 hour and WGA (Far Red 647, Invitrogen, catalog no. W32466) for 10 minutes in the dark. MCF-7 cells were stained with Calcein (Green 488) for 30 minutes, tumor cells and $CD8^+$ T cells were suspended at 12,500 × 10 μL and 25,000 × 10 μL in serum-free RPMI and put on ice for 10 minutes. Target cells and effector cells were then mixed together at a ratio of 1:2 and spun at 200 rpm for 5 minutes, then put on a poly-d-lysine coated glass bottom microwell dishes (catalog no. P35GC-1.0-14-C, MatTek Corporation). Images were acquired every minute for 30 minutes using an LSM 780 laser scanning confocal microscope (Zeiss) equipped with an EC-Plan-Neoflouar 40×/0.75 DIC (air). Particle count was performed using Fiji software (RRID:SCR_002285). Segmentation and manual thresholding were used to distinguish lysotracker-positive particles from background. Only cells with individual vesicles were selected to avoid false quantification created by vesicle aggregation. An average of 10 to 12 cells per image were used for particle counting. Four images used for

each condition (siControl vs. siNKG7). The open-source Fiji plugin Trackmate was used to perform single particle tracking (23). Track length and velocity (distance per time) were determined for lysotracker-positive vesicles in $CD8^+$ T cells in contact with tumor cells or contact-free. Two independent experiments were performed for each condition and three regions were randomly selected for time-lapse imaging (approximately 10 $CD8^+$ T cells per field of view).

Cas9/RNP transfection into human primary $CD8^+$ T cells

$CD8^+$ T cells were isolated from healthy donors, expanded by placing them on a 6-well plate precoated with 1 μg/mL anti-CD3 (clone OKT3, catalog no. 317326, BioLegend) and anti-CD28 (clone CD28.2, catalog no. 302934, BioLegend), and cultured in RPMI with 10% FBS, 100 IU/mL penicillin, 100 mg/mL streptomycin, and 2 mmol/L L-glutamine supplemented with 100 IU/mL recombinant human IL2 (see Supplementary Table S4 for reagent details).

Cas9/RNP complex was prepared and transfected into primary human $CD8^+$T cells as previously described (24). Equimolar amount of *NKG7*-specific CRISPR RNA (crRNA; GGGACCGGCAGAGCTCCATG; IDT) and trans-activating crispr RNA (tracrRNA; IDT) were mixed, incubated at 95°C for 5 minutes, and cooled down to room temperature. Four hundred and fifty picomoles of annealed crRNA-tracrRNA was mixed with 180 pmol of purified Cas9 protein (Alt-R s.p. Cas9 Nuclease V3, IDT, catalog no. 1081059) and incubated at room temperature for 10 minutes, creating the Cas9/RNP complex. Prepared Cas9/RNP complex was transfected into human $CD8^+$ T cells using a 4D nucleofector system (Lonza). 10×10^6 purified $CD8^+$ T cells were resuspended in 40 μL of P2 nucleofection solution (catalog no. V4XP-2032, Lonza) and mixed with Cas9/RNP complex. Cells with mixture were then nucleofected using program EH-100. Following transfection, cells were transferred into prewarmed complete RPMI with 100 IU/mL IL2 and rested. Seven days posttransfection, cells were stimulated and expanded on a tissue-culture plate precoated with 1 μg/mL of anti-CD3 (clone OKT3) and 1 μg/mL of anti-CD28 (clone CD28.2). All experiments were performed 14 to 21 days postactivation.

Transfection of human cells with *NKG7* mRNA

PBMC's from patients with melanoma were preserved with CryoStor (catalog no. 07952, StemCell) and thawed in complete RPMI containing 10% FBS, rhIL2: 10 U/mL, rhIL15: 10 ng/mL, and rhIL7: 10 ng/mL, and kept at 37°C overnight. The next morning, viable cells were transfected with control mRNA or *NKG7* mRNA. *NKG7* mRNA was prepared by Tri-Link based on NCBI reference sequence NM_005601. Control mRNA was CleanCap OVA mRNA, also from Tri-Link (catalog no. L-7610). Final mRNA concentration for transfection was 200 μg/mL in a 20-μL volume of P3 Buffer (Lonza Kit, catalog no. V4XP-3024) and program FI-115 on the 4D Nucleofector (Lonza) was used. $CD8^+$ T cells from healthy donors were freshly isolated and transfected the same day with either Control mRNA or *NKG7* mRNA (final mRNA concentration of 100 μg/mL in a 100-μL volume of P3 Buffer and program FI-115 on the 4D Nucleofector. Following transfection, cells were transferred to RPMI media (no FBS, no cytokines) for recovery. After 4 hours, warmed media was added such that each well contained RPMI with 10% FBS, rhIL2: 10 U/mL, rhIL15: 10 ng/mL, and rhIL7: 10 ng/mL. The next morning, soluble anti-CD3 (5 μg/mL; catalog no. 555336, BD Pharmingen) and anti-CD28 (5 μg/mL; catalog no. 555725, BD Pharmingen) were added for activation, with or without anti–PD-1/PD-L1 blockade (atezolizumab or pembrolizumab at 20 μg/mL) for 72 hours. Calcein assay was used to measure cytotoxicity as described above. For the *NKG7* mRNA rescue experiment, $CD8^+$ T cells transfected with Cas9/RNP were expanded for 19 to 21 days before transfection with *NKG7* mRNA. After mRNA transfection, cells were rested for 2 days before degranulation assay.

Degranulation assay

Expanded $CD8^+$ T cells and P815 cells were washed and resuspended in complete RPMI at 2.5 to 5×10^6 cells/mL. Anti-human CD3 (clone OKT3) was added to P815 cells at 2.5 to 5 μg/mL (target). Hundred microliters of $CD8^+$ T cells ($0.25–0.5 \times 10^6$ cells) was then added to same number of target and cells were incubated at 37°C for multiple times. At each time, cells were collected, labeled with Zombie Aqua viability dyes in PBS according to the manufacturer's instruction (BioLegend, catalog no. 423101), and stained using the following antibodies in FACS buffer (1% FBS, 1 mmol/L EDTA, 0.09% NaN_3 in PBS): FITC antimouse CD16/32, PerCP anti-human CD8, and PE anti-human CD107a (antibody details in Supplementary Table S3). After staining, cells were washed in PBS and fixed with 1% PFA in PBS. All samples were acquired on a BD FACSCanto II instrument with FACSDiva software. Percentage of $CD107a^+$ population among $CD8^+CD16/32^-$ population was examined using a FlowJo software (RRID:SCR_008520; version 9.96).

Calcium flux measurement using indo-1 AM

$CD8^+$ T cells from healthy donors were isolated and transfected with siRNA or mRNA as described above. Cells were harvested at a density of 1×10^6/mL and labeled with Indo-1 AM (5 μmol/L; catalog no. 565879, BD Pharmingen) at 37 °C for 30 minutes. Cells were washed with complete RPMI and incubated in complete RPMI for another 30 minutes at 37 °C. Finally, cells were suspended and kept in 37°C water bath before acquisition on an LSR II cytometer (BD Biosciences) running FACSDiva v6.1.3 software (RRID:SCR_001456). After baseline acquisition for 1 minute, the analogue of nicotinic acid, adenine dinucleotide phosphate (NAADP-AM; 10 μmol/L; catalog no. 21000, AAT Bioquest) was added and sample collection immediately resumed. In addition, we used trans-Ned-19 (an inhibitor of NAADP pathway; 10 μmol/L, Enzo Life Sciences, catalog no. ALX-270–503-M001) or Nigericin (an ionophore agent that depletes acidic Ca^{2+} stores; 10 μmol/L, Sigma, catalog no. SML1779) in culture medium 30 minutes before the addition of NAADP-AM to test effects on calcium release at basal level and induced by NAADP-AM. Flow data was analyzed by FlowJo, using the kinetic analyzer function (FlowJo, LLC).

Mouse studies

The Mayo Clinic Institutional Animal Care and Use Committee (IACUC) approved all animal experiments and mice were maintained under pathogen-free conditions in the animal facility at Mayo Clinic.

Transfection of mouse cells with *NKG7* mRNA

Spleens were harvested from OT-1 transgenic mice [C57BL/6-Tg (TcraTcrb)1100Mjb/J, Jackson Laboratory] and processed to single cell. Cells were then divided into aliquots of 10×10^6 cells/15 mL tube and spun down at $200 \times g$ for 10 minutes. Each pellet was then resuspended in 100 μL of nucleofection media (P3 Lonza kit, catalog no. V4XP-3024) containing either control mRNA (EGFP) or murine *NKG7* mRNA (8.28 ug/10×10^6 cells) and nucleofected using the 4D nucleofector system (Lonza) on program DN-100. *NKG7* mRNA was prepared by Tri-Link from NCBI reference sequence: NM_024253. Control mRNA was Tri-Link CleanCap EGFP mRNA (L7601). Following transfection, cells were transferred to RPMI media (no FBS, no cytokines) for recovery. After 4 hours, warmed RMPI was added such that each well contained 10% FBS, rhIL2: 10 U/mL, rhIL15: 10 ng/mL, and rhIL7: 10 ng/mL. The next morning, 1 μg/mL $OVA_{257–264}$ peptide

(catalog no. A5503, Sigma) was added for activation. Forty-eight hours after stimulation, cells were collected, counted and prepared for *in vitro* and *in vivo* assays.

To measure *NKG7* mRNA levels after 48 hours of activation, cells from three separate OT-1 mice were transfected as described above, activated, then collected in RLT buffer (Qiagen, catalog no. 79216) and processed using the Qiagen RNeasy Plus Mini Kit according to the manufacturer's instructions (catalog no. 74134). The RT reaction was completed using SuperScript III Reverse Transcriptase (catalog no. 18080–400, Invitrogen) with 125 ng of RNA template per sample. qRT-PCR analysis was completed using a Quant-Studio 3 Real-Time PCR System (Applied Biosystems) and TaqMan Fast Advanced Master Mix (catalog no. 444455, Applied Biosystems). Taqman assays included β-actin (Mm00607939–s1) and NKG7 (Mm01203147_g1), both from Applied Biosystems. All samples were run in triplicate. Relative expression was calculated using the $2^{-\Delta Ct}$ method.

Mouse calcein release cytotoxicity assay

Cells from whole spleen of OT-1 transgenic mice were transfected with control or *NKG7* mRNA, as described above. EL-4 mouse T-cell lymphoma cells were incubated with 1 μg/mL of $OVA_{257–264}$ peptide in RPMI media (no FBS) for 1 hour at 37°C. EL-4 cells were then washed twice with HBSS and labeled with Calcein-AM (5 μmol/L; incubation at 37°C in dark, 30 minutes, shaking occasionally). Following calcein-labeling, cells were again washed twice with HBSS and then resuspended at 1×10^5/mL in RPMI (no FBS). EL-4 cells and activated OT-1 cells were then mixed together at indicated target to effector ratios in RPMI without FBS, and seeded into the wells of a 96-well U-bottom plate. Remaining steps of calcein assay protocol and percent cytotoxicity calculations were identical to those listed above (see "Calcein release cytotoxicity assay").

Mouse *in vivo* treatment of tumors

0.5×10^6 B16-OVA cells suspended in 100 μL of sterile PBS were injected SubQ into C57BL/6 WT mice (The Jackson Laboratory, catalog no. 000664). Cells from whole spleen of OT-1 transgenic mice were transfected with control or *NKG7* mRNA, as described above, then activated for 48 hours with $OVA_{257–264}$ peptide prior to injection. On day 6 and day 13 of B16-OVA tumor growth, 1×10^6 of the activated OT-1 cells were injected into each mouse (peritumoral injection). Perpendicular tumor measurements were taken twice per week by calipers. Mice were euthanized if tumors became ulcerated or grew beyond 200 mm^2 in size, in compliance with animal care guidelines. For experiments testing combination antibody and OT-1 treatment, mice and cells were prepared as above, but mice were treated with either anti–PD-1 alone (clone G4, 100 μg/mouse; Millipore Sigma, catalog no. mabc1132), or anti–PD-1 in combination with OT-1 T cells transfected with either control or *NKG7* mRNA. Antibody was given on day 5 and day 11 of tumor growth. 1×10^6 OT-1 cells were given on days 6 and 12 of tumor growth.

Transcription factor analysis/ETS1 studies

Promoter *in silico* prediction

The DNA sequence located 500 bps upstream of *NKG7* (chr19:51,371,620-51,372,654) was extracted from UCSC Genome Browser (RRID:SCR_005780) from Human Dec. 2013 (GRCh38/hg38) reference genome. The virtual laboratory PROMO's (http://alggen.lsi.upc.es/cgi-bin/promo_v3/promo/promoinit.cgi?dirDB=TF_8.3) predictive software was used to generate a list of potential transcription factors that could bind the promoter sequence (dissimilarity margin of ≤ 5%). An additional search was conducted using P-Match software (http://gene-regulation.com) using 1,000 bps upstream of *NKG7* and the same reference genome. All hits were then cross-referenced against the scRNA-seq data sets to determine if the transcripts for these candidate transcription factors could be detected in the $CD8^+$ T cells. CEBPB, ETS1, REL, STAT4, and YY1 had detectable expression and were therefore selected for initial knockdown in Hut78 via siRNA nucleofection.

siRNA nucleofection

siRNA knockdown was completed in Hut78 or primary $CD8^+$ T cells using Lonza P3 Primary 4D Nucleofection Kit (catalog no. V4XP-3024) and Lonza 4D Nucleofector (see Supplementary Table S5 for siRNA catalog numbers). A pulse code of DN100 was used for the Hut78 cell line and code FI-115 was used for primary cells. Following transfection, cells were transferred to RPMI (no FBS, no cytokines) for recovery. After 4 hours, warmed media was added such that each well contained RPMI with 10% FBS, rh IL2: 10 U/mL, rh IL15: 10 ng/mL, and rh IL7: 10 ng/mL. The cells were then collected 48 hours after nucleofection in RLT buffer from the Qiagen RNeasy Plus Mini Kit (catalog no. 74134), followed by RNA isolation using the kit and reverse transcription using SuperScript III Reverse Transcriptase kit (catalog no. 18080-400, Invitrogen). Two hundred and twenty nanograms of RNA template was used per sample for the Hut78 reverse transcription reactions and 80 to 450 ng of RNA template was used per sample for the $CD8^+$ primary T-cell reactions due to varying RNA yields from primary T cells, but all samples were normalized to a housekeeping gene. qRT-PCR analysis was then completed using a Quant-Studio 3 Real-Time PCR System (Applied Biosystems) and SYBR green reagents (Invitrogen, catalog no. A25742). qRT-PCR primer sequences used are listed in Supplementary Table S6. All samples were run in triplicate. Relative expression was calculated using the $2^{-\Delta Ct}$ method.

ChIP-qPCR

Thermo Fisher Scientific Pierce Magnetic ChIP Kit (catalog no. 26157) was used per the manufacturer's protocol. MNase digestion timing was 15 minutes at 37°C for 4×10^6 cells. Sonication was completed using a Diagenode Biorupter with for 12 cycles, 30 seconds on/30 seconds off, at 4°C. Chromatin was incubated with Ets1 antibody (catalog no. 14069, Cell Signaling Technology) or 2-μL rabbit IgG (provided in the Magnetic ChIP Kit) overnight at 4 °C. After DNA recovery, quantification was completed with the QuantStudio 3 Quant-Studio 3 Real-Time PCR System and SYBR green reagents. Primer sequences used are listed in Supplementary Table S6.

Calcein assay

ETS1 siRNA or control siRNA was transfected into primary $CD8^+$ T as described above. Cells were stimulated with anti-CD3/anti-CD28 beads 24 hours after nucleofection. Following 48 hours of activation, cells were washed, counted, and combined with calcein-labeled MCF-7 target cells. Calcein assay and percent cytotoxicity calculations were completed as described above (see "Calcein release cytotoxicity assay").

Statistical analysis

The statistical tests performed are stated within the figure legends. Analysis of scRNA-seq data was performed as stated above. The statistical analysis for all other data was performed using Graphpad Prism (RRID:SCR_002798) v8.4.3 or later. Bar height represents mean, and error bars are SE of the mean, unless otherwise stated.

Data availability statement

scRNA-seq data has been deposited at the Gene Expression Omnibus (GEO; RRID:SCR_005012) under accession number GSE164237. Raw data for all other graphs shown have been submitted in Data File S1. Any other data can be obtained upon request.

Results

NKG7 expression decreased in CTLs of nonresponders to anti–PD-1 therapy

To identify gene expression levels linked to effective CTL killing, we isolated $CD8^+$ T cells from the peripheral blood of patients with advanced stages of melanoma who received anti–PD-1 therapy (**Fig. 1A**; Supplementary Table S2). Matched samples from BL and 12 weeks PT from 2 complete responders (R-1 and R-2) and two nonresponders (NR-1 and NR-2) were compared using scRNA-seq analysis. UMAP clustering of gene expression profiles from all eight samples identified four cell subsets: naïve-like, effector, effector exhausted (KLRB1), and a cluster high in mitochondrial gene expression (**Fig. 1B** and **C**). The first three of these clusters exhibited substantial overlap with those reported by Fairfax and colleagues (11), indicating these broad phenotypes are consistent across studies of human peripheral $CD8^+$ T cells.

The highest expression levels of genes encoding known cytolytic molecules [i.e., granulysin (GNLY); perforin-1(PRF1); granzyme H (GZMH); granzyme B (GZMB)] were all associated with the effector cluster (**Fig. 1D**), which was chosen for further analysis. We hypothesized that these are likely the peripheral CTLs shown to replenish the tumor-infiltrating $CD8^+$ T cells upon treatment with immune checkpoint inhibitors (8, 9). Thus, any differences between responders and nonresponders in this cell subset may ultimately affect clinical outcome. We found that the effector population was represented in all patients and its relative proportion in comparison with the total $CD8^+$ T-cell profile did not change within each individual between BL and pos-treatment timepoints (**Fig. 1E**). We then completed differential gene expression analyses and looked for gene expression changes that occurred posttreatment relative to baseline within each individual, i.e., a paired (PT vs. BL) integration analysis for each patient. Among those changes, we asked what differentiated responders from nonresponders (**Fig. 1F**). We found 46 genes differentially expressed by both nonresponder samples and 30 genes differentially expressed by both responder samples (Supplementary Table S7). Among the genes upregulated in both nonresponders were *TCF7*, *CCR7*, and *NELL2*, all of which are associated with naive and early-differentiated memory T cells. Genes upregulated in both responders included effector-related genes *GZMH*, *GZMM*, *GZMA*, and *CCL5*, as well as *KLRG1*, which is known to be expressed on antigen-experienced, fully differentiated effector $CD8^+$ T cells (25). Both responders also upregulated *TIGIT*, an immune checkpoint with an ITIM domain and suppressive function that upregulated in peripheral $CD8^+$ T cells of responders to anti–PD-1 therapy (26). However, we were most interested in those genes showing opposite trends in responders versus nonresponders and found one gene satisfying this criterion: *NKG7* was upregulated in the effector cells of the two responders and downregulated in the two nonresponders by 12 weeks PT (**Fig. 1G–I**). Thus, we found that although all patients harbored peripheral effector T cells, those T cells were not all equally effective in eliminating tumors as evidenced by the clinical response. Our initial dataset suggested that appropriate expression of NKG7 in cytotoxic $CD8^+$ T cells could be important for antitumor T-cell activity, particularly in the context of anti–PD-1 therapy.

Expansion of $CD8^+$ T-cell clones is indicative of antigen recognition, and the number of large $CD8^+$ T-cell clones in peripheral blood samples correlates with response to anti–PD-1-therapy (11). Whether molecular differences exist between these large clones in responders versus nonresponders has not been shown. Using an additional set of patient samples ($n = 2$ responders, $n = 2$ nonresponders; paired samples from BL and PT) and scRNA-seq analyses, we found that unsupervised clustering yielded 4 clusters identical to the first set of patient samples, shown in **Fig. 1B**, along with one small additional cluster, "LYZ," which may represent a group of T cells with capacity for antimicrobial function, or possibly a small number of natural killer (NK) cells/macrophages (**Fig. 2A**; refs. 27–29). Because this set of scRNA-seq included both gene expression and TCR α/β sequencing, we were able to compare the top five largest $CD8^+$ T-cell clones in each sample ("largest" meaning clones with the highest number of identical TCR sequences represented among all T cells sequenced for each individual at each timepoint) (**Fig. 2A–C**). In both responders and nonresponders, these large clones were predominantly composed of the effector phenotype with a cytotoxic profile (GNLY, effector cluster; **Fig. 2D**). The large clones from responders, however, exhibited higher expression of genes associated with T-cell cytotoxicity, including *NKG7* (**Fig. 2E** and **F**). We did additional analyses to determine which specific clones were expanded after therapy as opposed to baseline. These were not necessarily the largest clones, but they did increase in size upon anti–PD-1 treatment. Again, we found that the most expanded clone (**Fig. 2G**) and the top five most expanded clones (**Fig. 2H**) in responders exhibited higher expression of *NKG7* versus the expanded clones in nonresponders. Thus, both scRNA-seq cohorts revealed a correlation between NKG7 expression in cytotoxic $CD8^+$ T cells and response to anti–PD-1 therapy.

We next sought to corroborate the *NKG7* gene expression differences between responders and nonresponders at the protein level. The chemokine receptor CX3CR1 marks a population of peripheral $CD8^+$ T cells of the effector memory phenotype that are responsive to anti–PD-1/L1 therapy (30–32). We found a significant increase in the frequency of $CX3CR1^+CD8^+$ T cells that expressed NKG7 as compared with $CX3CR1^-CD8^+$ T cells (**Fig. 3A**). In addition, we observed a decreased frequency of $CX3CR1^+CD8^+$ cells expressing NKG7 in nonresponders to anti–PD-1 therapy, as compared with responders, at both the baseline and posttreatment timepoints (**Fig. 3B**).

As our initial studies had been in peripheral blood, we next considered whether NKG7 expression in tumor biopsies was associated with treatment response. Although NKG7 has been measured via RNA-based methods in bulk tumor samples, NKG7 protein expression has never been visualized within human tissues. Thus, we used IHC staining to confirm that NKG7 was expressed within lymphocytes in both normal lymphoid and tumor tissues (**Fig. 3C**). We then examined NKG7 expression in a set of primary tumor biopsies ($n = 47$; melanoma and NSCLC) in which bulk RNA-seq was performed. We found that prior to anti–PD-1/L1 treatment, nonresponders had lower levels of *NKG7* mRNA expression when compared with responders (**Fig. 3D**). Further, the level of *NKG7* expression within the tumor at BL was reasonably predictive of response to immune checkpoint blockade (AUC = 0.86; **Fig. 3E**). Taken together, our RNA- and protein-based analyses suggest that the lack of appropriate expression of NKG7 in cytotoxic $CD8^+$ T cells may contribute to nonresponsiveness to anti–PD-1/L1 immunotherapy.

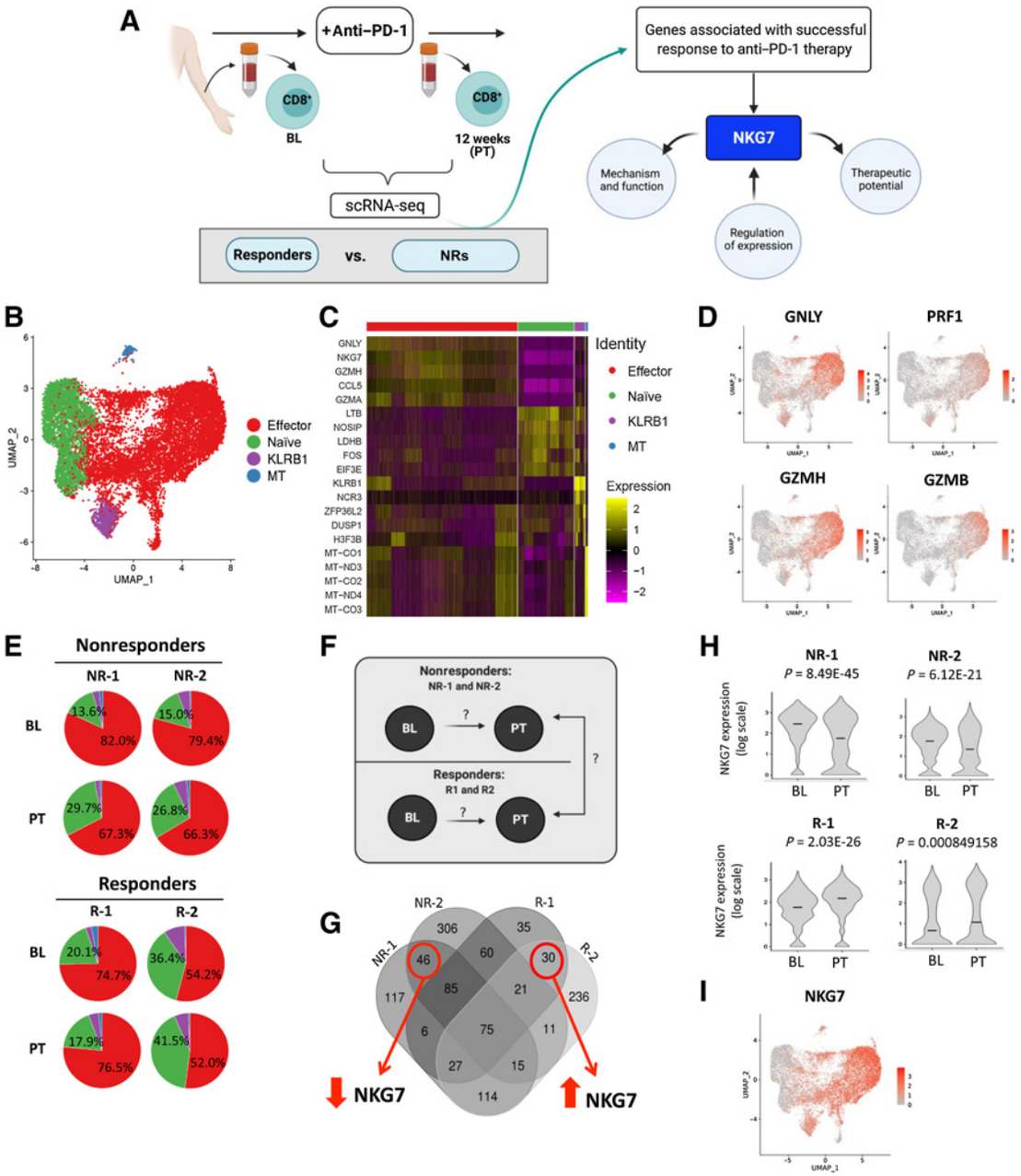

Figure 1.

Expression of *NKG7* mRNA decreases in the CD8$^+$ cytotoxic T cells of patients who fail anti–PD-1 therapy. **A,** Schematic overview of study. **B,** UMAP for cell expression profiles from eight samples: R-1, R-2, NR-1, and NR-2 at BL and PT timepoints. R-1-BL ($n = 767$ cells), R-1-PT ($n = 1{,}238$), R-2-BL ($n = 1{,}586$), R-2-PT ($n = 1{,}964$), NR-1-BL ($n = 1{,}631$), NR-1-PT ($n = 1{,}810$), NR-2-BL ($n = 2{,}525$), NR-2-PT ($n = 2{,}089$). UMAP resolution of 0.06 identifies four cell subsets: naïve-like (green), effector (red), effector exhausted (KLRB1, purple), and a cluster high in mitochondrial gene expression (blue). **C,** Heatmap of top 5 enriched gene markers for the clusters detected. **D,** Expression of four known cytolytic molecules. **E,** Pie charts show distribution of cells in the clusters of each dataset in the integration analysis of eight samples (BL, $n = 4$ patients; PT, $n = 4$), percentage shown for the major two clusters (colors are consistent with **B**). **F,** Analysis strategy. **G,** Venn diagram shows the number of differentially expressed genes (PT vs. BL) in the effector clusters of 4 patients, filtered by absolute value of fold change (FC) >1.1 and P value < 0.05. *NKG7* was the only gene with opposite trends in both nonresponders (NR; downregulated) and both responders (R; upregulated). **H,** Violin plots demonstrate *NKG7* expression in NR samples (downregulation) and R samples (upregulation). Bar, median. P values were obtained from differential gene expression analysis (PT vs. BL) at sample level. **I,** Feature plot of *NKG7* expression.

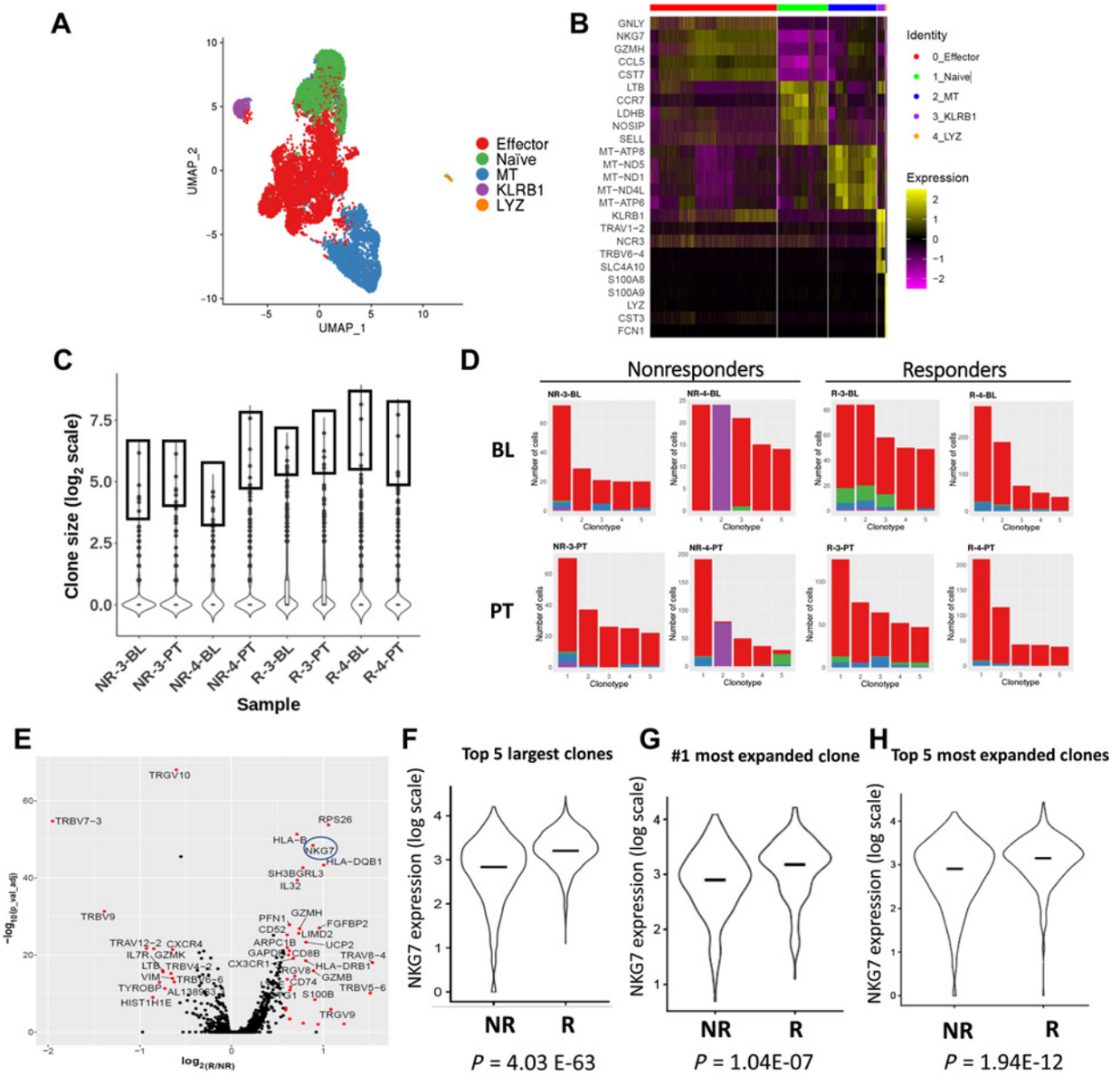

Figure 2.

Expanded CD8$^+$ T-cell clones of nonresponders to anti–PD-1 therapy exhibit lower expression of NKG7 mRNA. **A,** UMAP shows 5 cell subtypes from the integrated analysis of 8 samples: R-3, R-4, NR-3, and NR-4 datasets (BL, $n = 4$ patients; PT, $n = 4$). UMAP resolution of 0.08. The major four color-coded clusters are consistent with those in **Fig. 1B**. **B,** Heatmap of top five genes significantly enriched in each cluster. **C,** Violin plots show clone size distribution in each dataset. Boxes highlight the top five largest clones (by size) in each sample. **D,** Bar plots show cell distribution by cluster of the top five largest clones. Color-coded clusters are consistent with those in **A**. **E,** Volcano plot of gene expression ratio (R/NR) versus *P* value adjusted in the top five largest clones of BL samples. R/NR ratio (NKG7) = 1.85. **F,** Violin plot of *NKG7* expression in the top 5 largest clones of NR-3, NR-4 and R-3, R-4 samples ($n = 2{,}592$ cells). **G,** *NKG7* gene expression level in the most expanded clone from NRs versus Rs ($n = 933$ cells). Expanded clones were defined as being those with more cells in PT sample versus BL sample and have ≥ 10 cells in PT samples. **H,** *NKG7* gene expression level in the top five most expanded clones from NRs versus Rs ($n = 1{,}217$ cells). Note that R-4 only had 3 expanded clones detected. Bars in **F**–**H** are median. *P* values obtained from differential gene expression analysis (R vs. NR) using the same data.

Reduced NKG7 expression compromises CTL-mediated killing of tumor cells

The efficacy of cancer immunotherapy is ultimately dependent upon whether T cells can effectively kill tumor cells. Since lower levels of NKG7 were found in the effector CD8$^+$ T cells of nonresponders to anti–PD1 treatment, we next considered the possibility that NKG7 may play a functional role in T-cell cytolytic activity. This was plausible given the initial characterization of NKG7 (also named GMP-17) as a molecule associated with cytolytic granules (33, 34). In addition, a recent study using murine CD8$^+$ T cells found that NKG7 colocalizes with the known cytolytic granule-associated protein LAMP1 (CD107a) upon induction of cytolytic granule exocytosis and that

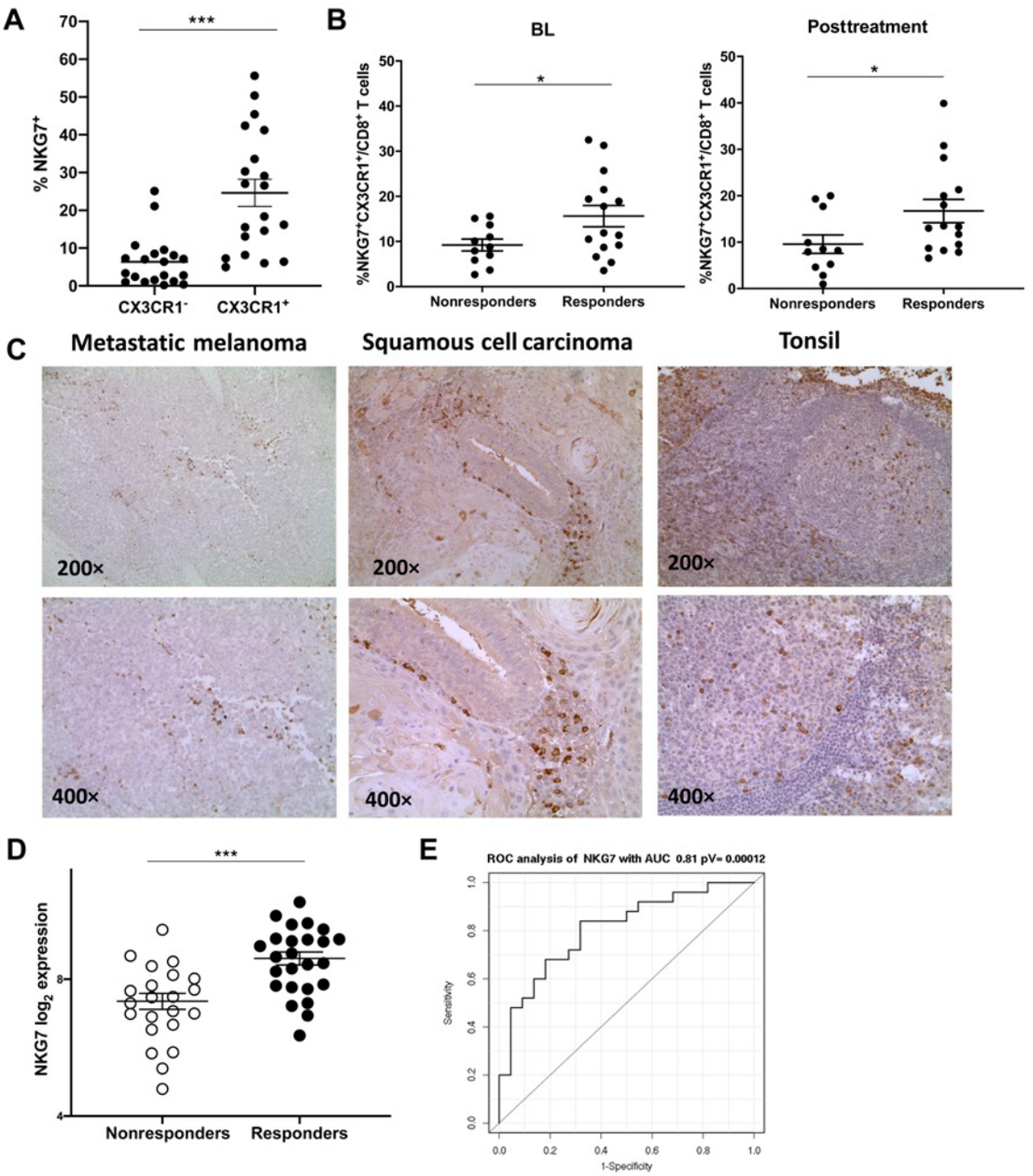

Figure 3.

Flow cytometry of peripheral blood samples and bulk RNA-seq of tumor biopsies confirm lower levels of *NKG7* expression in nonresponders to anti–PD-1 therapy. **A,** Percent of $CD8^+$ T cells positive for NKG7 was compared in the $CX3CR1^+$ versus $CX3CR1^-$ populations from PBMCs of patients with melanoma using flow cytometry (BL and PT samples used). Cells were first gated on $CD8^+CD11a^{hi}$ populations, then $CX3CR1^+$ versus $CX3CR1^-$ subsets. Mann–Whitney used ($n = 20$ patients; ***, $P < 0.001$, lines are mean and SEM). **B,** Percent of $CD8^+$ T cells double positive for $NKG7^+CX3CR1^+$ was compared between patients who eventually responded or progressed on anti–PD-1 therapy. BL and PT time points were analyzed separately. Unpaired *t* test was used ($n = 15$ responders, $n = 11$ non-responders; *, $P < 0.05$, lines are mean and SEM). **C,** Brown cytoplasmic staining is positive for NKG7; blue nuclear stain is hematoxylin. Staining positive in normal human tonsil, metastatic melanoma (met to small bowel), and squamous cell carcinoma (excised from tongue). **D,** Log_2 normalized *NKG7* mRNA expression in primary tumor biopsies according to response ($n = 25$ responders, $n = 22$ nonresponders). Unpaired *t* test used (***, $P < 0.001$, lines are mean and SEM). **E,** ROC curve for *NKG7* mRNA expression in the tumor biopsies of eventual responders versus nonresponders to anti–PD-1/L1 therapy ($n = 47$ patients as in **D**, AUC 0.81, ***, $P < 0.001$). Note that in the ROC curve, sensitivity represents the true positive rate (TPR) and specificity is 1– false positive rate (1-FPR). A random classifier that has no predictive value would give points lying along the diagonal (FPR = TPR).

knock-out of *NKG7* decreased NK cell–mediated cytotoxicity in mouse metastatic tumor models (35). We sought to corroborate these findings in primary human CD8$^+$ T cells.

Immunofluorescent staining confirmed that NKG7 is maintained in close proximity to CD107a and is somewhat associated with perforin in human cells (**Fig. 4A** and **B**). Notably, we found that depletion of *NKG7* by siRNA knockdown resulted in a significant reduction of T cell–mediated cytotoxicity (**Fig. 4C** and **D**; Supplementary Fig. S1A and S1B). To determine the mechanism by which decreased NKG7 expression results in reduced CD8$^+$ T cell–mediated cytotoxicity, we next quantified cytolytic granule release after NKG7 depletion. We found that CRISPR/Cas9-mediated KO of *NKG7* in primary human CD8$^+$ T cells resulted in a reduction in degranulation following T-cell stimulation (**Fig. 4E**; Supplementary Fig. S1C). We further confirmed that this was an NKG7-specific effect by restoring NKG7 expression to the *NKG7* KO cells (via *NKG7* mRNA transfection), which rescued the phenotype and restored degranulation to normal levels (**Fig. 4F** and **G**).

We next examined the interaction between tumor cells and CD8$^+$ T cells via electron microscopy. We observed direct cell–cell contact between T cells and tumor cells in both control and *NKG7* siRNA conditions (**Fig. 4H**). However, we noted a decreased number of cell

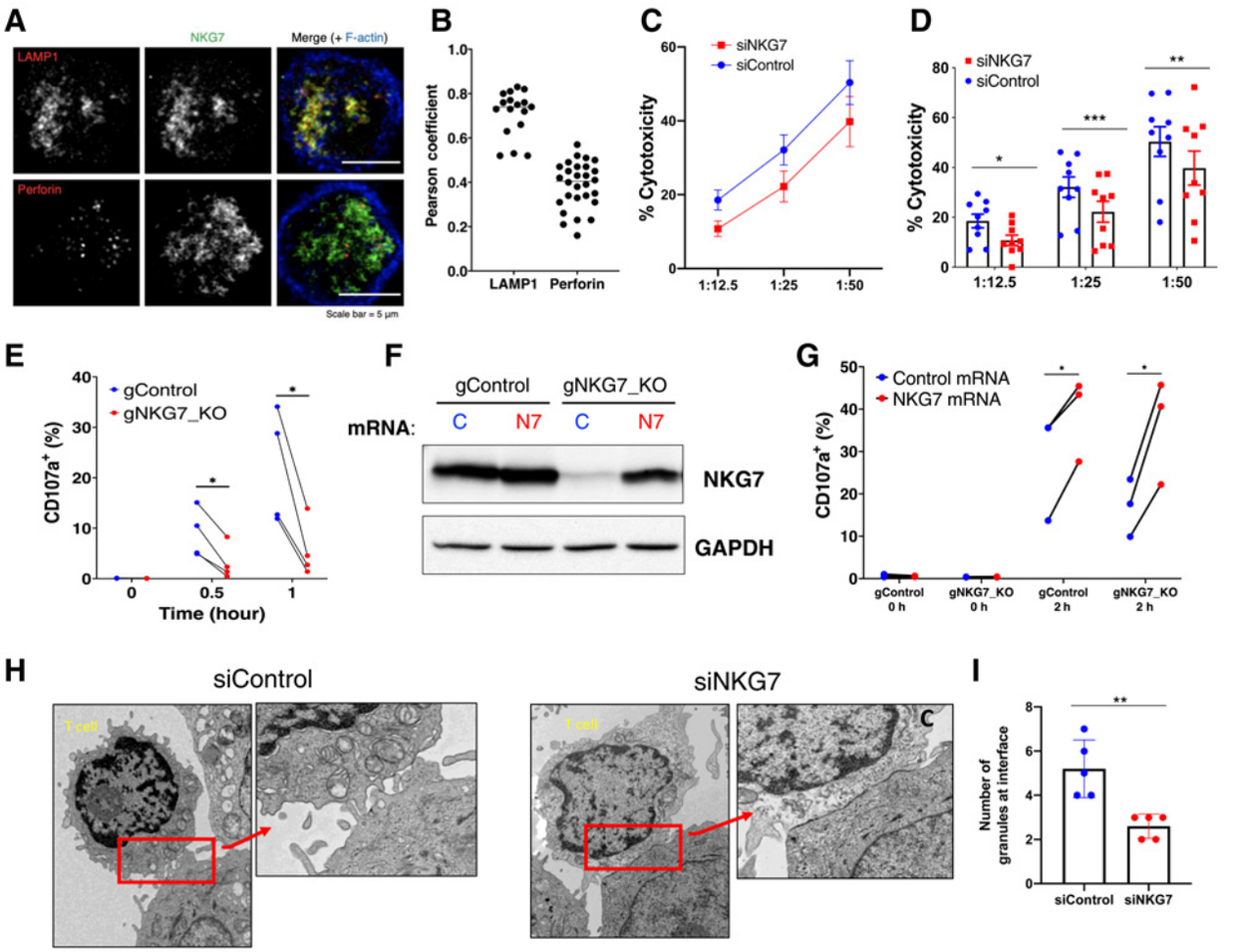

Figure 4.

Reduced NKG7 expression results in decreased CD8$^+$ T-cell killing of tumor cells. **A,** Activated primary human CD8$^+$ T cells stained for indicated proteins. **B,** Pearson Correlation Coefficient for colocalization with NKG7. Each dot represents an individual cell at high resolution. Line is median. **C,** CD8$^+$ T cells from healthy donors were transfected with control or *NKG7* siRNA, activated for 48 hours with anti-CD3/CD28, and then cocultured with calcein-labeled MCF-7 tumor cells at indicated target to effector ratios. After 4 hours, calcein release in supernatant was measured and percent cytotoxicity calculated. Symbols are mean; lines are SEM. Same data visualized as an *x,y* plot in **C**, dot plot in **D**. Paired *t* test ($n = 9$ separate donors; each dot is the average of triplicate wells). Bar height is mean; bars are SEM. **E,** CRISPR/Cas9 RNP complexes were used to knock-out *NKG7* from primary CD8$^+$ T cells isolated from peripheral blood of $n = 4$ healthy donors. Graph shows percentage of CD107a$^+$ cells among CD8$^+$CD16/32$^-$ population after coculture with activated P815 target cells. Paired *t* test, *, $P < 0.05$. **F,** Knock-out cells were transfected with either control or *NKG7* mRNA. Western blot (WB) confirms knock-out of *NKG7* in T cells from a representative donor (gNKG7_KO), as compared with cells from the same donor that did not receive the NKG7-specific control siRNA (gControl). Western blot also shows that the addition of *NKG7* mRNA (red "N7") resulted in increased abundance of NKG7 protein in both gControl and gNKG7_KO cells. GAPDH loading control. Representative of 3 healthy donors. **G,** The activated gControl or gNKG7-KO CD8$^+$ T cells rescued with *NKG7* mRNA or control mRNA were used in test of their degranulation as in **E** at a 1:1 ratio. Dots are average of 3 healthy donors. Paired *t* test used. (*, $P < 0.05$). h, hours. **H,** TEM images of CD8$^+$ T cells from healthy donors transfected with siRNA, activated with anti-CD3/CD28, and then cocultured with MCF-7 tumor cells prior to analysis. Images are representative of 5 images/condition analyzed from 3 different donors. **I,** Number of granules within T cell at the T cell–tumor cell interface quantified (each dot is a separate image). Unpaired *t* test used (**, $P < 0.01$). Bar height is mean, and lines are SEM.

membrane extensions between T cells and tumor cells when T cells were transfected with *NKG7* siRNA. In addition, we observed small granules present within the presumed immune synapse between control siRNA–transfected T cells and the tumor cells, but fewer of these granules were present at the synapse within T cells that were deficient in NKG7 (**Fig. 4I**). This agreed with our CD107a results. We next considered whether there were fewer granules overall present (per cell) when *NKG7* was depleted. A broader examination of the electron microscopy images revealed that the morphology and densities of cytolytic granules were similar in control and *NKG7* knockdown $CD8^+$ T cells (Supplementary Fig. S2A), but the overall number of cytolytic granules was decreased in *NKG7* knockdown $CD8^+$ T cells compared with control cells (Supplementary Fig. S2B). In addition, we found the granules were dispersed with certain distances in control $CD8^+$ T cells, but there were more aggerated granules in *NKG7* KO $CD8^+$ T cells (Supplementary Fig. S2C).

To better characterize the dynamics of granule trafficking, we prepared cocultures of tumor cells and $CD8^+$ T cells and monitored them using real time confocal microscopy. $CD8^+$ T cells were labeled with lysotracker to visualize lysosomal vesicles and wheat germ agglutinin (WGA), which binds to glycoproteins of the cell membrane (**Fig. 5A**). Labeled T cells were then cocultured with calcein-stained MCF-7 tumor cells. We observed fewer cytotoxic granules per cell in the *NKG7* siRNA cells versus control siRNA cells (**Fig. 5B**). In terms of cytotoxicity, control $CD8^+$ T cells began killing tumor cells within 10 minutes of coculture, with high speed and long-distance movement of granules toward the tumor–immune cell interface within those T cells as they attacked their targets. In contrast, *NKG7* siRNA–transfected $CD8^+$ T cells engaged tumor cells, but their granules showed reduced speed and shorter distance movements within the cytoplasm (**Fig. 5C** and **D**). Thus, we conclude that reduced NKG7 affects the overall number of granules within T cells, and that the granules that remain display decreased velocity and trafficking distance upon tumor cell target engagement.

Exocytosis and trafficking of cytolytic granules is Ca^{2+}-dependent (36), and the four membrane-spanning domains of NKG7 are structurally similar to the γ subunit of an L-type voltage-gated calcium channel (34). Thus, we next measured and compared the intracellular Ca^{2+} levels of $CD8^+$ T cells with or without *NKG7* siRNA transfection using the calcium-sensitive fluorescent indicator Indo-1 AM. NAADP-AM, induces Ca^{2+} release from acidic organelles, such as cytolytic granules (37, 38). For this assay, T cells from healthy donors were labeled with Indo-1 AM and baseline fluorescence acquisition was performed for 1 minute via flow cytometry. Then, NAADP-AM was added, and acquisition immediately resumed to visualize peak calcium flux. When NKG7 was depleted from $CD8^+$ T cells, we found that NAADP-AM–induced Ca^{2+} release was significantly decreased (**Fig. 5E**). Conversely, increased expression of NKG7 resulted in an increased peak calcium flux after NAADP-AM stimulation (**Fig. 5F**). We found in the *NKG7* mRNA–transfected WT T cells there was already more calcium detected in the cytoplasm at baseline before addition of NAADP-AM, although it was not a significant increase compared with control mRNA–transfected T cells (**Fig. 5F**, BL). This raises the possibility that NKG7 overexpression may cause a release of calcium from *other*, nongranule, sources of calcium into the cytoplasm.

To test this possibility, we treated control or *NKG7* mRNA transduced $CD8^+$ T cells with Nigericin, an ionophore agent that depletes acidic Ca^{2+} stores and dissipates Ca^{2+} release–initiated by NAADP-AM. Treatment with Nigericin suppressed the Ca^{2+} release–initiated by NAADP-AM in both control cells and NKG7 overexpressing cells (**Fig. 5G**), but the decrease of Ca^{2+} release was not significant in $CD8^+$ T cells with NKG7 overexpression (**Fig. 5H**). Similarly, when we treated those $CD8^+$ T cells with Trans-Ned-19, an inhibitor of the NAADP pathway, the Ca^{2+} release initiated by NAADP-AM was inhibited in both control cells and NKG7 overexpressing cells, but was not significant in NKG7 overexpressing cells (**Fig. 5G** and **H**). The two inhibitors did not significantly decrease the basal level of calcium in the NKG7 overexpressing cells compared with control cells. Taken together, our results suggest that NKG7 may promote Ca^{2+} release from both NAADP-affected acidic organelles (like cytolytic granules) and NAADP-unaffected sources (perhaps the endoplasmic reticulum).

Collectively, these data point to a role for NKG7 in regulating calcium release from lysosomal vesicles that impacts cytolytic granule trafficking and release within cytotoxic $CD8^+$ T cells.

NKG7 mRNA therapy increases the antitumor cytotoxicity of $CD8^+$ T cells

Because reduced levels of NKG7 compromised the cytolytic efficiency of $CD8^+$ T cells, we next hypothesized that by increasing expression of NKG7 we could enhance the cytolytic activity of effector $CD8^+$ T cells, resulting in better response to immune checkpoint inhibitors. In the last several decades, technology has advanced such that immune cells can be effectively modified via transfection with mRNA that is produced *in vitro* (39), with the particular advantage that this mRNA can be transfected into nonproliferative primary T cells and presents low risk of genome mutagenesis. This opens the door for innovative therapeutic strategies designed to modulate therapeutic targets within T cells directly, through the addition of mRNA.

We found that transfection of primary human $CD8^+$ T cells with *NKG7* mRNA resulted in increased levels of NKG7 protein (Supplementary Fig. S3A). To test the functional impact of NKG7 overexpression in the most clinically relevant samples, we next transfected PBMCs from patients with melanoma who failed to respond to anti–PD-1 treatment (**Fig. 6A**). The addition of *NKG7* mRNA significantly increased T-cell killing of melanoma tumor cells, and this effect was even more robust when combined with anti–PD-1 or anti–PD-L1 pretreatment (**Fig. 6B** and **C**). To confirm this was a T cell–specific effect, we also transfected isolated $CD8^+$ T cells from healthy donors with *NKG7* mRNA. We found that increasing NKG7 expression led to increased T-cell cytotoxicity (Supplementary Fig. S3B). Although the T-cell cytotoxicity of *NKG7* mRNA–transduced $CD8^+$ T cells increased significantly in culture with anti–PD-L1 compared with control mRNA cells, this increase was not significant in culture with media only or with anti–PD-1, suggesting that *NKG7* mRNA transfection may not further benefit T-cell responses to anti–PD-1 therapy in healthy donors who may already have sufficient basal levels of NKG7.

To demonstrate that overexpression of NKG7 could improve $CD8^+$ T-cell killing in an antigen-specific manner, we transfected OT-1 transgenic T cells with murine *NKG7* mRNA or control (GFP) mRNA (**Fig. 6D**). OT-1 cells with increased NKG7 expression exhibited enhanced cytolytic ability when challenged with EL4 cells pulsed with OVA peptide *in vitro* (**Fig. 6E**). In addition, *NKG7* mRNA–transfected OT-1 cells suppressed the aggressive growth of B16-OVA cells *in vivo* significantly better than control OT-1 cells (**Fig. 6F–H**). Using a similar ACT model, we also tested combination treatment with anti–PD-1 antibody and OT-1 cells. Although combination anti–PD-1 and *NKG7* mRNA–transfected OT-1 treatment significantly decreased tumor growth and increased overall survival versus no treatment controls, the B16-OVA model was already responsive to anti–PD-1 therapy alone and the addition of *NKG7* mRNA–transfected OT-1s did not add further benefit (Supplementary

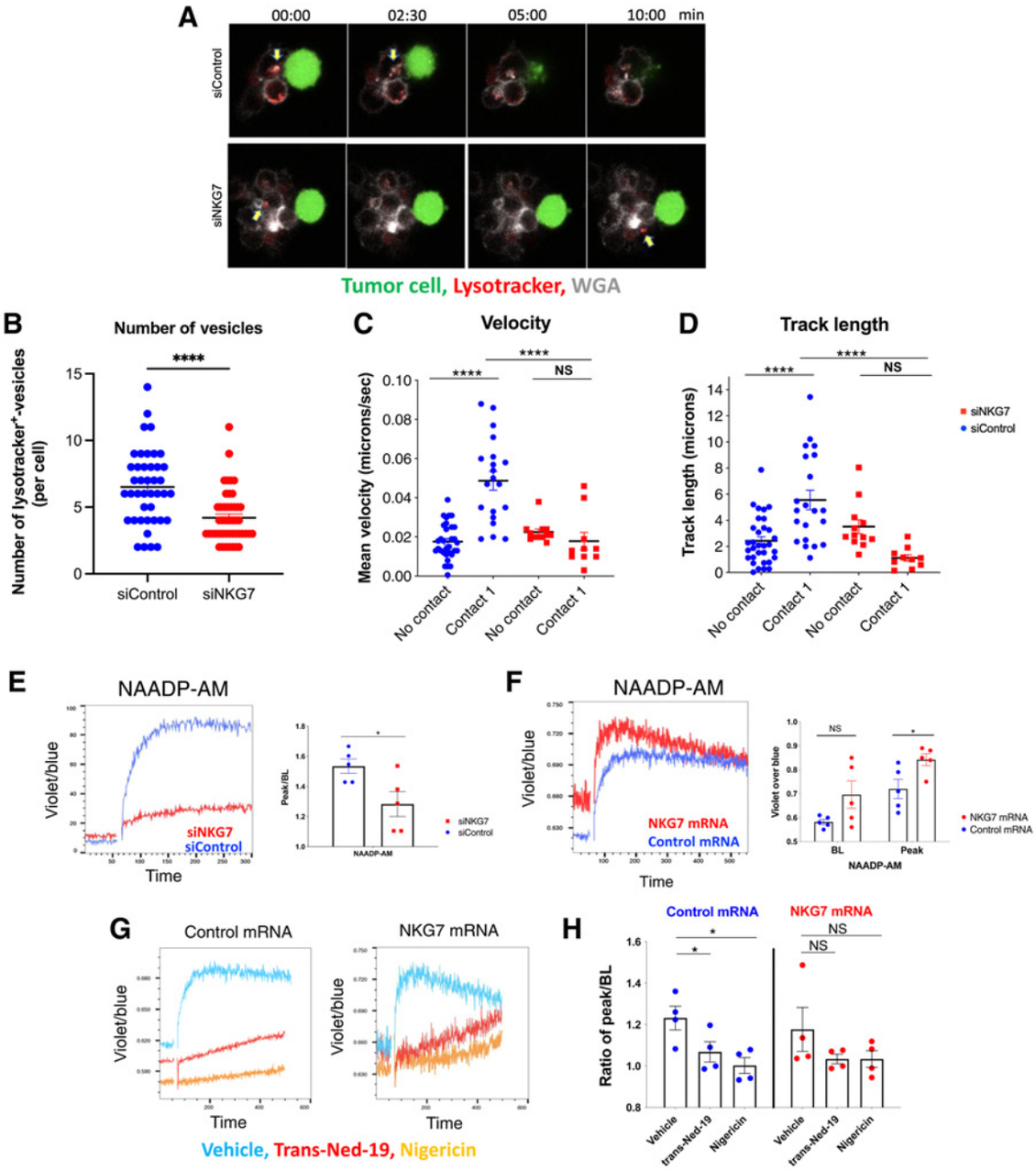

Figure 5.

Reduced NKG7 expression compromises cytolytic granule number, trafficking, and calcium flux in $CD8^+$ T cells. **A,** Representative images from real-time imaging. Min, minutes. **B,** Count of lysotracker positive particles per individual T cell. Average of 10 to 12 cells per image, four images per condition (siControl vs. siNKG7). Mann–Whitney test used. **C** and **D,** Mean velocity and track length measured for individual granules within T cells in contact with MCF-7 (Contact 1) or contact-free (no contact). Each dot represents mean velocity and track length per cell analyzed. Images were acquired every minute for 30 minutes. Two independent experiments were performed, and data combined. Three regions/condition were randomly selected for time-lapse imaging ($n \geq 10$ granules/condition, $n = 2$ healthy donors). One-way ANOVA with Tukey test. Sec, second. **E,** Calcium flux assay. T cells from healthy donors were transfected with control or *NKG7* siRNA, then labeled with Indo-1 AM. Using a flow cytometer, baseline fluorescence acquisition was acquired for 1 minute. Then, NAADP-AM was added and acquisition immediately resumed. Representative flow data are shown as violet (405 nm) over blue (510 nm). Quantification shown at right as ratio of peak/BL ($n = 5$ healthy donors). Unpaired *t* test. **F,** Calcium flux assay using cells transfected with control or *NKG7* mRNA. Representative flow data are shown as violet (405 nm) over blue (510 nm). Quantification shown at right ($n = 5$ healthy donors). Data separated into BL and peak for each sample. Unpaired *t* test used. **G** and **H,** As in **F**, inhibitors (Trans-Ned-19 or Nigericin) were added 30 minutes before stimulation with NAADP-AM. Data are presented as ratio of peak/BL calcium flux with 4 donors. *, $P < 0.05$, **, $P < 0.01$, ***, $P < 0.001$, ****, $P < 0.0001$. Bars, mean; error bars, SEM throughout. NS, not significant.

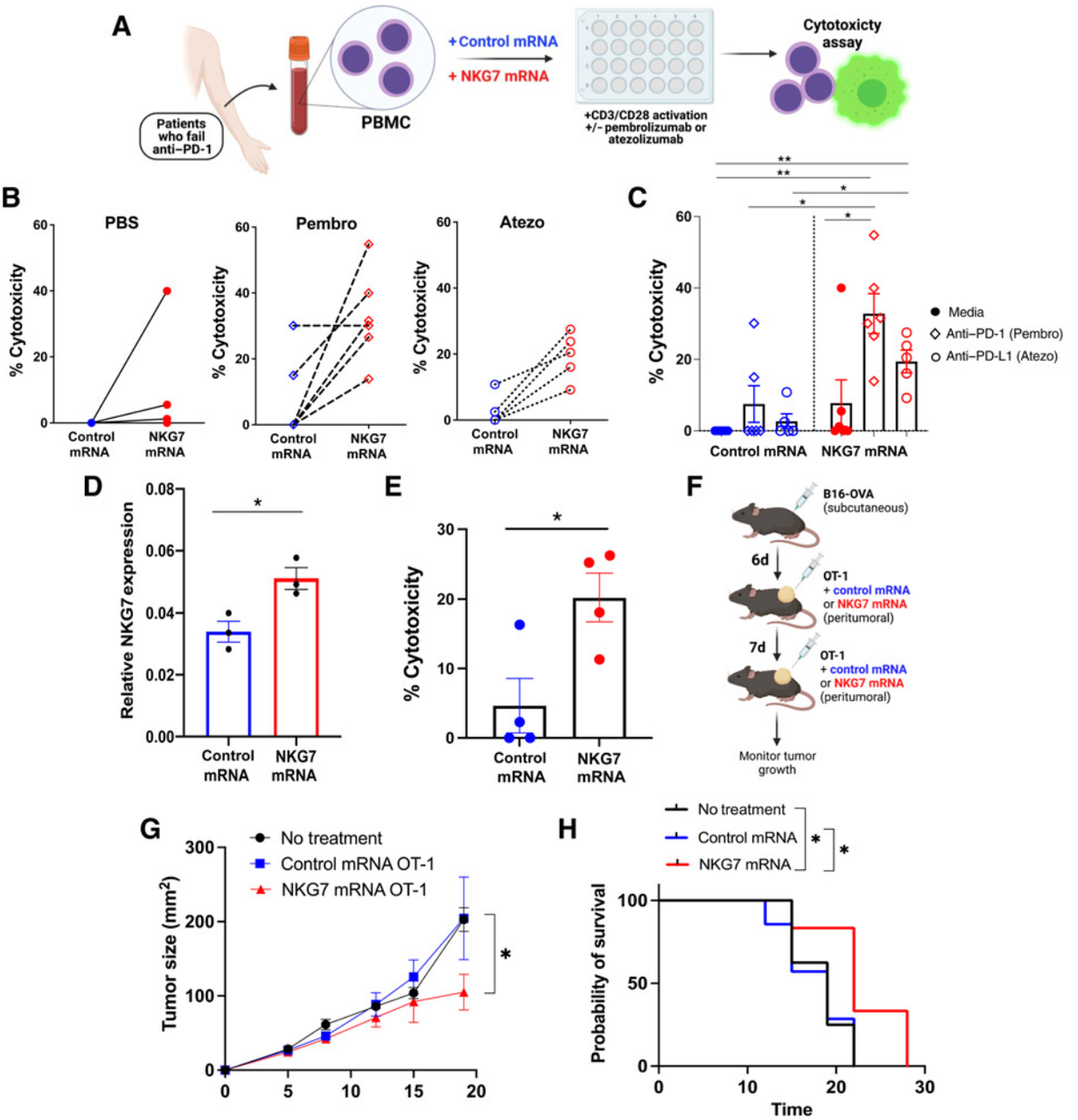

Figure 6.

NKG7 mRNA transfection increases the antitumor cytotoxicity of $CD8^+$ T cells and improves response to immune checkpoint inhibitors. **A,** Schematic of experimental protocol. **B,** Percent cytotoxicity calculated after calcein release assay. Lines connect paired samples from same individual. Target cells were human melanoma cell line A375, assayed at 1:20 target to effector ratio. **C,** Summary graph of data from **B**. Mann–Whitney test used ($n = 6$ patients for media, pembrolizumab; $n = 5$ of those also run with atezolizumab; each dot is average of triplicate wells). **D,** Cells isolated from the spleen of OT-1 transgenic mice were transfected with control mRNA or *NKG7* mRNA, then activated with $OVA_{257–264}$ peptide. After 48 hours of activation, remaining *NKG7* mRNA levels were quantified via qRT-PCR. Each dot represents average of triplicate wells for a single mouse ($n = 3$ mice). Unpaired *t* test used. **E,** Cells transfected and activated as in **D** were cocultured with calcein-labeled EL4 tumor cells pulsed with $OVA_{257–264}$ peptide at target to effector ratio of 1:10. Unpaired *t* test used ($n = 4$ separate experiments; each dot is the average of four replicate wells in a single experiment). **F,** Schematic of *in vivo* experimental protocol. d, days. **G,** Average growth curves for each group ($n = 8$ untreated, $n = 7$ control OT-1, $n = 6$ NKG7 OT-1). Unpaired *t* test used. **H,** Survival curve of mice to humane endpoint. Log-rank (Mantel–Cox) test. Data are representative of three separate *in vivo* experiments. *, $P < 0.05$, **, $P < 0.01$. Bars, mean; error bars, SEM throughout.

Fig. S4). This indicates that the endogenous T cells already had sufficient NKG7, as they were able to respond to anti–PD-1. Thus, the addition of *NKG7* mRNA is likely to be therapeutically indicated only in settings where NKG7 levels are reduced or depleted, as in nonresponders to checkpoint blockade.

The transcription factor ETS1 is a negative regulator of *NKG7* expression

Little is known regarding upstream mechanisms that could be responsible for regulating *NKG7* transcription. Thus, we performed *in silico* analysis of binding motifs contained within the *NKG7* promoter sequence to identify putative transcriptional regulators (**Fig. 7A**; Supplementary Fig. S5). We then used siRNA to knock down these transcription factor candidates in Hut78 T cells and found that knockdown of the transcription factor ETS1 resulted in an increase in *NKG7* mRNA expression (**Fig. 7B**). ETS1 is known to regulate genes involved in both T- and NK-cell differentiation and activation (40–42). Further, members of the ETS1 transcription factor family bind to the promoters of effector T cell–relevant genes such as *PERFORIN* and *CFOS* to regulate their expression (43–45), so we next considered whether ETS1 might bind to the promoter of *NKG7*. Using ChIP-qPCR, we confirmed that ETS1 was indeed associated with the *NKG7* promoter in $CD8^+$ T cells isolated from healthy human donors (**Fig. 7C**). We then knocked down *ETS1* in additional healthy donor primary $CD8^+$ T-cell samples and observed an increase in NKG7 expression at both the mRNA and protein levels (**Fig. 7D–F**). Finally, to determine whether this modulation had functional significance, we transfected $CD8^+$ T cells from healthy donors with *ETS1* siRNA or control siRNA followed by activation with anti-CD3/CD28 and found that ETS1 siRNA–transfected cells were better able to kill MCF-7 target cells in the calcein-based cytotoxicity assay (**Fig. 7G**), as we hypothesized, given the higher levels of NKG7 that result from *ETS1* knockdown.

Using our scRNA-seq dataset (from **Fig. 1**), we next completed analysis of "RNA velocity." RNA velocity leverages the relative ratio between intronic (unspliced) and exonic (spliced) mRNAs in scRNA-seq data to infer the rate of change in transcript abundance and thus predict the future transcriptional state for a cell (18). The underlying assumption in this analysis was that genes are initially transcribed in an unspliced manner and then spliced, such that observed intronic reads can be interpreted as corresponding to nascently transcribed mRNAs. Using the UMAP projection from **Fig. 1B**, we found that the overall flow of cell velocity started from the naive cells and continued over to effector cells (black arrows in **Fig. 7H**). More specifically, we found the velocity of *NKG7* transcription gradually increases in effector cells (**Fig. 7I**). In contrast, *EST1* gene expression demonstrated positive velocity of ETS1 in naive cells, but decreased velocity in effector cells (**Fig. 7I**). Thus, our scRNA-seq data from patient samples further supports our findings that *NKG7* is subject to regulation by ETS1 in peripheral $CD8^+$ T cells. We conclude that ETS1 is a transcriptional repressor of *NKG7* expression and suggest that interventions that modulate ETS1 may represent another opportunity for optimizing $CD8^+$ T-cell cytotoxicity.

Discussion

This work establishes a causal connection between appropriate expression of NKG7 and the cytolytic capacity of $CD8^+$ T cells, particularly in the setting of immune checkpoint inhibitor therapy. Through the use of scRNA-seq technology, we were able to assess gene expression differences in the effector T cells of responders versus nonresponders to anti–PD-1 treatment across multiple time points within individual patients. This revealed that *NKG7* expression was reduced in the cells of nonresponding patients, which was confirmed at the protein level. Our subsequent studies highlighted the functional role of NKG7 in cytolytic $CD8^+$ T-cell activity, as decreased NKG7 levels resulted in significantly less tumor-cell killing. This is in agreement with a recent report by Ng and colleagues, which showed that KO of *NKG7* can compromise antitumor immunity in mouse models of metastatic tumor growth (35). Our study goes further to assess the role of NKG7 in human $CD8^+$ T cells and provides evidence that *NKG7* mRNA therapy enhances the cytolytic function of T cells from patients who may not have sufficient NKG7.

Insufficient neoantigen expression (mutation burden) by the tumor or lack of PD-L1 on the tumor cell surface (46–50) are among the explanations proposed for why anti–PD-1 therapy may fail. Our study concludes that a deficiency in an intrinsic component of cytolytic T cells can limit the effectiveness of immunotherapy. In agreement with our finding, *NKG7* was among the list of transcripts found to be differentially expressed in the peripheral $CD8^+$ T cells of responders versus nonresponders to anti–PD-1 therapy by Fairfax and colleagues (11). However, their bulk RNA-seq analysis generated a list of thousands of differentially expressed transcripts, making it difficult to pinpoint NKG7 as a critical component among so many options in the context of effector T cells. Our scRNA-seq and approach to analysis yielded fewer hits, directing us early-on to NKG7 as a correlate with response. However, we were surprised when we completed the initial functional studies and found that rather than just serving as a biomarker for treatment outcome, NKG7 was necessary to drive optimal $CD8^+$ T-cell cytotoxicity. Why and how NKG7 plays such a dominant role in modulating cytolytic activity is still not fully clear, but we showed that modulation of this one protein was able to alter granule number, trafficking, and release. It may be that NKG7 is not only working locally at the level of each granule, but also is working more globally to affect broader cytoplasmic or nuclear signals. Our finding that the level of NKG7 within $CD8^+$ T cells was directly linked to the amount of calcium flux at baseline and after NAADP-stimulation supports this model, given the importance of calcium as a second messenger in a variety of T-cell processes.

We observed that NKG7 expression declined at the protein level upon activation of $CD8^+$ T cells (Supplementary Fig. S1B and Supplementary Fig. S3A). This suggests a potential self-restraining mechanism inherent to cytotoxic T cells meant to prevent extensive killing activity that could damage normal tissues. This is supported by findings that NKG7 may be upregulated in lymphocytes in the setting of autoimmune conditions, organ transplant rejection, and other pathologies (51–53). However, within the tumor microenvironment, where effector $CD8^+$ T cells are confronted with rapidly dividing tumor cells, T cells may need more persistent expression of NKG7 to maintain highly efficient tumor-cell killing capacity and effectively overcome the exponential growth of the tumor.

We show that at the transcription level, ETS1 negatively regulates *NKG7* expression, but there are likely a number of other factors that influence *NKG7* expression that remain to be determined. In the current study, to bypass the need to control transcription itself, we piloted an mRNA transfection approach. Translationally, this would allow T cells to be modified and then adoptively transferred to improve immune therapy (54, 55). As mRNA does not require a nuclear phase for efficient expression, it is an attractive means for achieving rapid and sufficient expression of NKG7 in nondividing cells (like human primary T cells). The use of mRNA instead of DNA as a therapeutic substance is also advantageous due to the absent risk of insertional mutagenesis. Though the short half-life of mRNA could be a potential therapeutic disadvantage in some cases, in the current context, the

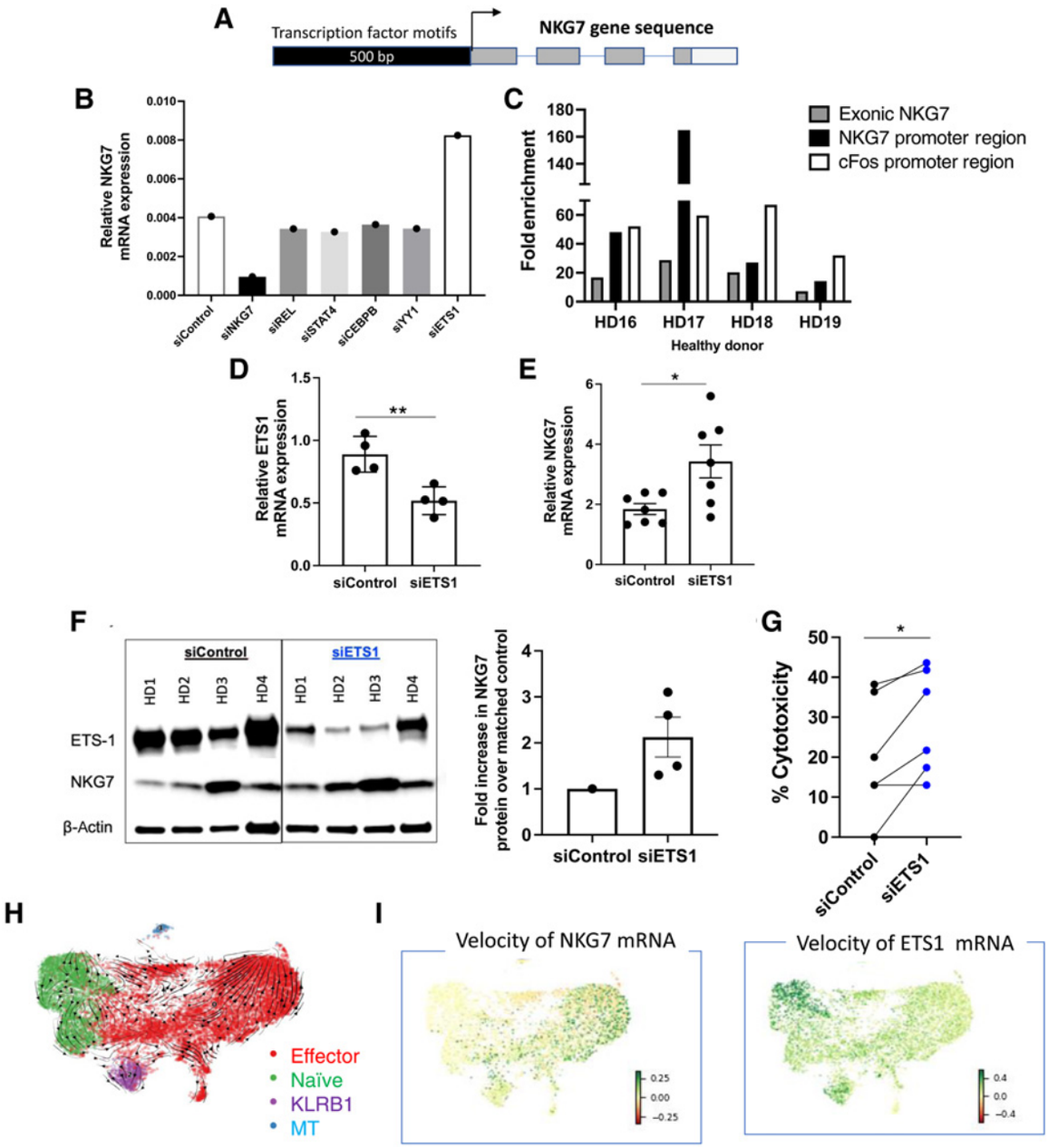

Figure 7.

The transcription factor ETS1 is a negative regulator of *NKG7* expression. **A,** Diagram of *NKG7* gene (exons shown in gray) and 500-bp sequence upstream of the transcriptional start site (black). **B,** *NKG7* mRNA expression quantified via qRT-PCR in Hut78 cells at 48 hours posttransfection of siRNA. Dot represents average of triplicate qRT-PCR assays from a single donor. **C,** ChIP-qPCR was performed on $CD8^+$ T cells from healthy donors; ETS1 antibody pull-down followed by qPCR using primers specific for either exons 1 and 2 of *NKG7* (gray bars) or the *NKG7* promoter (black bars). Primers for the cFos promoter (open bars), were used as a positive control. Data is represented as fold enrichment over nonspecific Rabbit IgG control ($n = 4$ donors). **D,** Primary $CD8^+$ T cells from healthy donors were transfected with control siRNA or *ETS1* siRNA and *ETS1* mRNA expression quantified at 24 hours posttransfection via qRT-PCR ($^{**}P = 0.0031$, paired *t* test; $n = 4$ donors). **E,** $CD8^+$ T cells from healthy donors were transfected as in **D** and collected at 48 hours posttransfection. qRT-PCR detected relative levels of *NKG7* mRNA ($^{*}P = 0.02$, paired *t* test; $n = 7$ donors). Bars, mean; error bars, SEM**. F,** Primary $CD8^+$ T cells analyzed via Western blot. β-actin loading control. Densitometry quantification at right represented as fold increase in NKG7 over each donor's control-transfected sample ($n = 4$ donors). Control values were normalized to 1. **G,** $CD8^+$ T cells transfected with control siRNA or *ETS1* siRNA, activated with anti-CD3/CD28, and then cocultured with MCF-7 tumor cells in a calcein-based cytotoxicity assay ($^{*}P = 0.025$, paired *t* test; $n = 6$ donors; lines connect paired samples from same donor). **H,** Velocity vector analysis of scRNA-seq data, overlaid on UMAP from **Fig. 1B**. Arrows indicate the extrapolated future state of peripheral $CD8^+$ T cells. Cells are colored by cell type. **I,** Velocity of *NKG7* and *ETS1* mRNA with positive velocity indicating upregulation (dark green), or negative velocity indicating downregulation (dark red) of the gene.

transient nature of mRNA may avoid the unwanted effects of permanent overexpression of NKG7 within cytotoxic T cells that could lead to normal tissue damage.

We endeavored to use human patient samples whenever possible to ensure our findings were relevant to the clinical setting. However, the paucity of live $CD8^+$ T cells that can be recovered from frozen patient PBMC samples prevented us from being able to specifically isolate patient $CD8^+$ T cells prior to transfection with *NKG7* mRNA. This limitation was addressed with the use of healthy donors' purified $CD8^+$ T cells as a proof of concept, but we plan to include further testing in freshly isolated patient samples in future studies. To test our hypothesis *in vivo*, we used a preclinical mouse model. However, the OT-1 T cells used in this assay had normal levels of NKG7 expression prior to mRNA transfection. This may not reflect the state of $CD8^+$ T cells in clinical nonresponders, which our studies suggest have a reduced amount of NKG7 both at BL and posttherapy. This limitation prevented us from determining if there is a dose-dependent effect of the *NKG7* mRNA *in vivo*. In addition, we found that the B16-OVA tumor model was responsive to anti–PD-1 therapy at BL. Although the adoptive transfer of NKG7 overexpressing OT-1 T cells combined with anti–PD-1 was just as effective, we were unable to detect any additional benefit from the combination treatment. With regard to our proposed therapeutic approach, pretreatment assessment of NKG7 levels would further direct clinicians to a subset of patients that would likely fail immune checkpoint inhibitor therapy alone, but would benefit from our proposed gene therapy, i.e., transduction of *NKG7* mRNA in combination with immune checkpoint inhibitors. To that end, our future studies will provide additional detection tools to quantify the expression of NKG7 in peripheral T cells and in tumor tissues to further validate NKG7 as a novel biomarker that can direct rational combination therapy.

In summary, our results indicate that anti–PD-1 immune checkpoint blockade fails to optimize $CD8^+$ cytotoxic T-cell response if the intrinsic, cytolytic granule-associated factor NKG7 is not sufficiently expressed. We further show that NKG7 is critical for cytotoxic $CD8^+$ T-cell antitumor activity due to its role in cytolytic granule trafficking and release. Finally, we demonstrate that *NKG7* mRNA transfection can improve cytotoxic $CD8^+$ T-cell killing of tumor cells, representing a new therapeutic target that could increase response rates to cancer immunotherapy, including immune checkpoint inhibitor and adoptive T-cell therapy.

Authors' Disclosures

D.D. Monie reports grants from NCI during the conduct of the study. A.S. Mansfield reports other support from Genentech, AbbVie, Bristol Myers Squibb, Janssen, and Shanghai Roche Pharmaceuticals and grants from Mark Foundation, NIH, and DoD outside the submitted work, and is a nonremunerated director of the Mesothelioma Applied Research Foundation. S.N. Markovic reports grants from NIH during the conduct of the study, as well as grants from Bristol Myers Squibb and Sorrento Therapeutics outside the submitted work. S.S. Park reports grants from MacroGenics and NCI, and other support from AstraZeneca outside the submitted work. M.C. Liu reports other support from Eisai, Genentech, Merck, Novartis, Seattle Genetics, Tesaro, AstraZeneca, Pfizer, and Genomic Health outside the submitted work. G. Vasmatzis reports other support from WholeGenome LLC outside the submitted work. No disclosures were reported by the other authors.

Authors' Contributions

T. Wen: Conceptualization, formal analysis, investigation, methodology, writing–review and editing. **W. Barham:** Conceptualization, formal analysis, investigation, methodology, writing–original draft, writing–review and editing. **Y. Li:** Conceptualization, software, formal analysis, methodology, writing–review and editing. **H. Zhang:** Investigation, writing–review and editing. **J.K. Gicobi:** Investigation, writing–review and editing. **J.B. Hirdler:** Investigation, writing–review and editing. **X. Liu:** Investigation, methodology, writing–review and editing. **H. Ham:** Resources, formal analysis, investigation, writing–review and editing. **K.E. Peterson Martinez:** Investigation, writing–review and editing. **F. Lucien:** Investigation, writing–review and editing. **R.R. Lavoie:** Investigation, writing–review and editing. **H. Li:** Software, formal analysis, writing–review and editing. **C. Correia:** Software, formal analysis, writing–review and editing. **D.D. Monie:** Software, formal analysis, writing–review and editing. **Z. An:** Investigation, writing–review and editing. **S.M. Harrington:** Investigation, writing–review and editing. **X. Wu:** Resources, investigation, writing–review and editing. **R. Guo:** Resources, writing–review and editing. **R.S. Dronca:** Resources, writing–review and editing. **A.S. Mansfield:** Resources, writing–review and editing. **Y. Yan:** Resources, writing–review and editing. **S.N. Markovic:** Resources, writing–review and editing. **S.S. Park:** Resources, writing–review and editing. **J. Sun:** Resources, writing–review and editing. **H. Qin:** Resources, writing–review and editing. **M.C. Liu:** Resources, writing–review and editing. **G. Vasmatzis:** Software, investigation, writing–review and editing. **D.D. Billadeau:** Resources, funding acquisition, investigation, writing–review and editing. **H. Dong:** Conceptualization, supervision, funding acquisition, methodology, writing–original draft, writing–review and editing.

Acknowledgments

We thank all the patients who generously contributed samples and participated in the study. We also acknowledge the Division of Medical Oncology at the Mayo Clinic for providing excellent patient care. This study was supported in part by the generosity of Mayo Clinic benefactors. We acknowledge the Genome Analysis Core at Mayo Clinic, Rochester, including technologists Vernadette A. Simon and Fariborz Rakhshan-Rohakhtar as well as supervisors Julie S. Lau, Samantha J. McDonough, and Mark Mutawe. We are grateful for the electron microscopy imaging service provided by Bing Huang and Scott I. Gamb at the Mayo Clinic Microscope and Cell Analysis Core. BioRender.com was used to create the graphics throughout the manuscript.

We acknowledge support from the Mayo Clinic Center for Individualized Medicine's IMPRESS program and High-Definition Therapeutics program (to H. Dong), the Mayo Clinic Center for Biomedical Discovery (to H. Dong), the Mayo Clinic Cancer Center's David F. and Margaret T. Grohne Cancer Immunology and Immunotherapy program (H. Dong, D.D. Billadeau), the Richard M. Schulze Family Foundation (to H. Dong), the Innovation Accelerator Awards program of the Office of Translation to Practice (OTP) at the Mayo Clinic Center for Clinical and Translational Science (CCaTS), NIH grant F30 CA250326 (to W. Barham), NIH grant F30 CA250122 (to D.D. Monie), National Institute of General Medical Sciences T32 GM65841 (to W. Barham and D.D. Monie), NIH grant R21 CA251923 (to A.S. Mansfield), NIH grant K12 CA 090628 (to Y. Yan), NIH grant R21 CA197878 (to H. Dong), NIH grant R01 AI095239 (to H. Dong), NIH grant R01 CA200551 (to H. Dong and S.S Park), and NIH grant R01 CA256927 (to H. Dong).

The publication costs of this article were defrayed in part by the payment of publication fees. Therefore, and solely to indicate this fact, this article is hereby marked "advertisement" in accordance with 18 USC section 1734.

Note

Supplementary data for this article are available at Cancer Immunology Research Online (http://cancerimmunolres.aacrjournals.org/).

Received July 7, 2021; revised October 19, 2021; accepted December 9, 2021; published first December 15, 2021.

References

1. Hellstrom I, Hellstrom KE, Pierce GE, Yang JP. Cellular and humoral immunity to different types of human neoplasms. Nature 1968;220:1352–4.
2. Dieckmann NM, Frazer GL, Asano Y, Stinchcombe JC, Griffiths GM. The cytotoxic T lymphocyte immune synapse at a glance. J Cell Sci 2016;129:2881–6.
3. Ham H, Billadeau DD. Human immunodeficiency syndromes affecting human natural killer cell cytolytic activity. Front Immunol 2014;5:2.
4. Pitt JM, Marabelle A, Eggermont A, Soria JC, Kroemer G, Zitvogel L. Targeting the tumor microenvironment: removing obstruction to anticancer immune responses and immunotherapy. Ann Oncol 2016;27:1482–92.

5. Gajewski TF, Schreiber H, Fu YX. Innate and adaptive immune cells in the tumor microenvironment. Nat Immunol 2013;14:1014–22.
6. Khunger M, Jain P, Rakshit S, Pasupuleti V, Hernandez AV, Stevenson J, et al. Safety and efficacy of PD-1/PD-L1 inhibitors in treatment-naive and chemotherapy-refractory patients with non-small-cell lung cancer: a systematic review and meta-analysis. Clin Lung Cancer 2018;19:e335–e48.
7. Zhang T, Xie J, Arai S, Wang L, Shi X, Shi N, et al. The efficacy and safety of anti-PD-1/PD-L1 antibodies for treatment of advanced or refractory cancers: a meta-analysis. Oncotarget 2016;7:73068–79.
8. Wu TD, Madireddi S, de Almeida PE, Banchereau R, Chen YJ, Chitre AS, et al. Peripheral T cell expansion predicts tumour infiltration and clinical response. Nature 2020;579:274–8.
9. Yost KE, Satpathy AT, Wells DK, Qi Y, Wang C, Kageyama R, et al. Clonal replacement of tumor-specific T cells following PD-1 blockade. Nat Med 2019;25:1251–9.
10. Kamphorst AO, Pillai RN, Yang S, Nasti TH, Akondy RS, Wieland A, et al. Proliferation of PD-1+ CD8 T cells in peripheral blood after PD-1-targeted therapy in lung cancer patients. Proc Natl Acad Sci U S A 2017;114:4993–8.
11. Fairfax BP, Taylor CA, Watson RA, Nassiri I, Danielli S, Fang H, et al. Peripheral CD8(+) T cell characteristics associated with durable responses to immune checkpoint blockade in patients with metastatic melanoma. Nat Med 2020;26:193–9.
12. Huang AC, Postow MA, Orlowski RJ, Mick R, Bengsch B, Manne S, et al. T-cell invigoration to tumour burden ratio associated with anti-PD-1 response. Nature 2017;545:60–5.
13. Ott PA, Bang YJ, Piha-Paul SA, Razak ARA, Bennouna J, Soria JC, et al. T-cell-inflamed gene-expression profile, programmed death ligand 1 expression, and tumor mutational burden predict efficacy in patients treated with pembrolizumab across 20 cancers: KEYNOTE-028. J Clin Oncol 2019;37:318–27.
14. Ayers M, Lunceford J, Nebozhyn M, Murphy E, Loboda A, Kaufman DR, et al. IFN-gamma-related mRNA profile predicts clinical response to PD-1 blockade. J Clin Invest 2017;127:2930–40.
15. Eisenhauer EA, Therasse P, Bogaerts J, Schwartz LH, Sargent D, Ford R, et al. New response evaluation criteria in solid tumours: revised RECIST guideline (version 1.1). Eur J Cancer 2009;45:228–47.
16. Butler A, Hoffman P, Smibert P, Papalexi E, Satija R. Integrating single-cell transcriptomic data across different conditions, technologies, and species. Nat Biotechnol 2018;36:411–20.
17. Stuart T, Butler A, Hoffman P, Hafemeister C, Papalexi E, Mauck WM 3rd, et al. Comprehensive integration of single-cell data. Cell 2019;177:1888–902.
18. La Manno G, Soldatov R, Zeisel A, Braun E, Hochgerner H, Petukhov V, et al. RNA velocity of single cells. Nature 2018;560:494–8.
19. Bergen V, Lange M, Peidli S, Wolf FA, Theis FJ. Generalizing RNA velocity to transient cell states through dynamical modeling. Nat Biotechnol 2020;38:1408–14.
20. Kalari KR, Nair AA, Bhavsar JD, O'Brien DR, Davila JI, Bockol MA, et al. MAP-RSeq: Mayo Analysis Pipeline for RNA sequencing. BMC Bioinformatics 2014;15:224.
21. Vasmatzis G, Wang X, Smadbeck JB, Murphy SJ, Geiersbach KB, Johnson SH, et al. Chromoanasynthesis is a common mechanism that leads to ERBB2 amplifications in a cohort of early stage HER2(+) breast cancer samples. BMC Cancer 2018;18:738.
22. Costes SV, Daelemans D, Cho EH, Dobbin Z, Pavlakis G, Lockett S. Automatic and quantitative measurement of protein-protein colocalization in live cells. Biophys J 2004;86:3993–4003.
23. Tinevez JY, Perry N, Schindelin J, Hoopes GM, Reynolds GD, Laplantine E, et al. TrackMate: an open and extensible platform for single-particle tracking. Methods 2017;115:80–90.
24. Seki A, Rutz S. Optimized RNP transfection for highly efficient CRISPR/Cas9-mediated gene knockout in primary T cells. J Exp Med 2018;215:985–97.
25. Voehringer D, Koschella M, Pircher H. Lack of proliferative capacity of human effector and memory T cells expressing killer cell lectinlike receptor G1 (KLRG1). Blood 2002;100:3698–702.
26. Simon S, Voillet V, Vignard V, Wu Z, Dabrowski C, Jouand N, et al. PD-1 and TIGIT coexpression identifies a circulating CD8 T cell subset predictive of response to anti-PD-1 therapy. J Immunother Cancer 2020;8:e001631.
27. Levitz SM, Mathews HL, Murphy JW. Direct antimicrobial activity of T cells. Immunol Today 1995;16:387–91.
28. Stenger S, Hanson DA, Teitelbaum R, Dewan P, Niazi KR, Froelich CJ, et al. An antimicrobial activity of cytolytic T cells mediated by granulysin. Science 1998;282:121–5.
29. De Biasi S, Gibellini L, Tartaro DL, Puccio S, Rabacchi C, Mazza EMC, et al. Circulating mucosal-associated invariant T cells identify patients responding to anti-PD-1 therapy. Nat Commun 2021;12:1669.
30. Yan Y, Cao S, Liu X, Harrington SM, Bindeman WE, Adjei AA, et al. CX3CR1 identifies PD-1 therapy-responsive CD8+ T cells that withstand chemotherapy during cancer chemoimmunotherapy. JCI Insight 2018;3:e97828.
31. Bottcher JP, Beyer M, Meissner F, Abdullah Z, Sander J, Hochst B, et al. Functional classification of memory CD8(+) T cells by CX3CR1 expression. Nat Commun 2015;6:8306.
32. Gerlach C, Moseman EA, Loughhead SM, Alvarez D, Zwijnenburg AJ, Waanders L, et al. The chemokine receptor CX3CR1 defines three antigen-experienced CD8 T cell subsets with distinct roles in immune surveillance and homeostasis. Immunity 2016;45:1270–84.
33. Turman MA, Yabe T, McSherry C, Bach FH, Houchins JP. Characterization of a novel gene (NKG7) on human chromosome 19 that is expressed in natural killer cells and T cells. Hum Immunol 1993;36:34–40.
34. Medley QG, Kedersha N, O'Brien S, Tian Q, Schlossman SF, Streuli M, et al. Characterization of GMP-17, a granule membrane protein that moves to the plasma membrane of natural killer cells following target cell recognition. Proc Natl Acad Sci U S A 1996;93:685–9.
35. Ng SS, De Labastida Rivera F, Yan J, Corvino D, Das I, Zhang P, et al. The NK cell granule protein NKG7 regulates cytotoxic granule exocytosis and inflammation. Nat Immunol 2020;21:1205–18.
36. Pores-Fernando AT, Zweifach A. Calcium influx and signaling in cytotoxic T-lymphocyte lytic granule exocytosis. Immunol Rev 2009;231:160–73.
37. Davis LC, Morgan AJ, Chen JL, Snead CM, Bloor-Young D, Shenderov E, et al. NAADP activates two-pore channels on T cell cytolytic granules to stimulate exocytosis and killing. Curr Biol 2012;22:2331–7.
38. Calcraft PJ, Ruas M, Pan Z, Cheng X, Arredouani A, Hao X, et al. NAADP mobilizes calcium from acidic organelles through two-pore channels. Nature 2009;459:596–600.
39. Zhao Y, Zheng Z, Cohen CJ, Gattinoni L, Palmer DC, Restifo NP, et al. High-efficiency transfection of primary human and mouse T lymphocytes using RNA electroporation. Mol Ther 2006;13:151–9.
40. Hollenhorst PC, Chandler KJ, Poulsen RL, Johnson WE, Speck NA, Graves BJ. DNA specificity determinants associate with distinct transcription factor functions. PLoS Genet 2009;5:e1000778.
41. Taveirne S, Wahlen S, Van Loocke W, Kiekens L, Persyn E, Van Ammel E, et al. The transcription factor ETS1 is an important regulator of human NK cell development and terminal differentiation. Blood 2020;136:288–98.
42. Cauchy P, Maqbool MA, Zacarias-Cabeza J, Vanhille L, Koch F, Fenouil R, et al. Dynamic recruitment of Ets1 to both nucleosome-occupied and -depleted enhancer regions mediates a transcriptional program switch during early T-cell differentiation. Nucleic Acids Res 2016;44:3567–85.
43. Glimcher LH, Townsend MJ, Sullivan BM, Lord GM. Recent developments in the transcriptional regulation of cytolytic effector cells. Nat Rev Immunol 2004;4:900–11.
44. Lacorazza HD, Miyazaki Y, Di Cristofano A, Deblasio A, Hedvat C, Zhang J, et al. The ETS protein MEF plays a critical role in perforin gene expression and the development of natural killer and NK-T cells. Immunity 2002;17:437–49.
45. Gangwar SP, Meena SR, Saxena AK. Purification, crystallization and preliminary X-ray crystallographic analysis of the ETS domain of human Ergp55 in complex with the cfos promoter DNA sequence. Acta Crystallogr Sect F Struct Biol Cryst Commun 2012;68:1333–6.
46. Garon EB, Rizvi NA, Hui R, Leighl N, Balmanoukian AS, Eder JP, et al. Pembrolizumab for the treatment of non-small-cell lung cancer. N Engl J Med 2015;372:2018–28.
47. Chow LQM, Haddad R, Gupta S, Mahipal A, Mehra R, Tahara M, et al. Antitumor Activity of pembrolizumab in biomarker-Unselected patients with recurrent and/or metastatic head and neck squamous cell carcinoma: results from the Phase Ib KEYNOTE-012 expansion cohort. J Clin Oncol 2016;34:3838–45.
48. Le DT, Uram JN, Wang H, Bartlett BR, Kemberling H, Eyring AD, et al. PD-1 blockade in tumors with mismatch-repair deficiency. N Engl J Med 2015;372:2509–20.
49. Yarchoan M, Albacker LA, Hopkins AC, Montesion M, Murugesan K, Vithayathil TT, et al. PD-L1 expression and tumor mutational burden are independent biomarkers in most cancers. JCI Insight 2019;4:e126908.

50. McGranahan N, Furness AJ, Rosenthal R, Ramskov S, Lyngaa R, Saini SK, et al. Clonal neoantigens elicit T cell immunoreactivity and sensitivity to immune checkpoint blockade. Science 2016;351:1463–9.
51. Khatri P, Roedder S, Kimura N, De Vusser K, Morgan AA, Gong Y, et al. A common rejection module (CRM) for acute rejection across multiple organs identifies novel therapeutics for organ transplantation. J Exp Med 2013;210: 2205–21.
52. Gate D, Saligrama N, Leventhal O, Yang AC, Unger MS, Middeldorp J, et al. Clonally expanded CD8 T cells patrol the cerebrospinal fluid in Alzheimer's disease. Nature 2020;577:399–404.
53. van Es LA, de Heer E, Vleming LJ, van der Wal A, Mallat M, Bajema I, et al. GMP-17-positive T-lymphocytes in renal tubules predict progression in early stages of IgA nephropathy. Kidney Int 2008;73:1426–33.
54. Foster JB, Barrett DM, Kariko K. The emerging role of In Vitro-transcribed mRNA in adoptive T cell immunotherapy. Mol Ther 2019;27:747–56.
55. Tchou J, Zhao Y, Levine BL, Zhang PJ, Davis MM, Melenhorst JJ, et al. Safety and efficacy of intratumoral injections of chimeric antigen Receptor (CAR) T cells in metastatic breast cancer. Cancer Immunol Res 2017;5:1152–61.